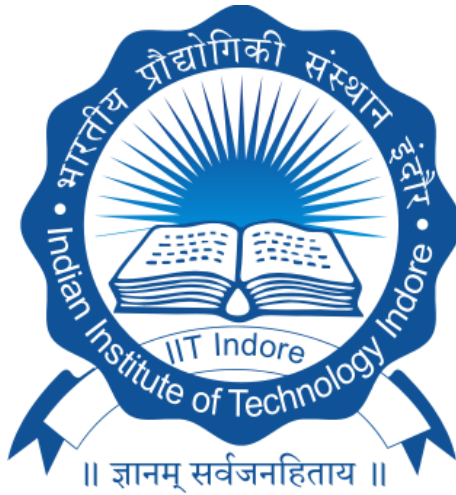


# **A CUBESAT FOR RFI DETECTION AND TETHERED INTERFEROMETER EXPERIMENT**

**M.Tech Thesis**

**By:  
Kundan Sahu**



**DEPARTMENT OF ASTRONOMY , ASTROPHYSICS AND  
SPACE ENGINEERING**

**INDIAN INSTITUTE OF TECHNOLOGY INDORE**

**May, 2024**

# **A CUBESAT FOR RFI DETECTION AND TETHERED INTERFEROMETER EXPERIMENT**

**A THESIS**

*Submitted in partial fulfillment of the  
requirements for the award of the degree  
of  
**M.Tech***

*by*  
**Kundan Sahu**



**DEPARTMENT OF ASTRONOMY , ASTROPHYSICS AND  
SPACE ENGINEERING**

**INDIAN INSTITUTE OF TECHNOLOGY INDORE**

**May, 2024**

**INDIAN INSTITUTE OF TECHNOLOGY INDORE**

**CANDIDATE'S DECLARATION**

I hereby certify that the work which is being presented in the thesis entitled “**A CubeSat for RFI detection and Tethered Interferometer Experiment**” in the partial fulfilment of the requirements for the award of the degree of MASTER OF TECHNOLOGY and submitted in the DEPARTMENT OF ASTRONOMY, ASTROPHYSICS, AND SPACE ENGINEERING, Indian Institute of Technology Indore, is an authentic record of my own work carried out during the time period from July 2022 to May 2024 under the supervision of Prof. Abhirup Datta. The matter presented in this thesis has not been submitted by me for the award of any other degree of this or any other institute.

*Kundan Sahu .*

**Kundan Sahu**

-----  
This is to certify that the above statement made by the candidate is correct to the best of my knowledge.

*Abhirup Datta*

24/05/2024

Supervisor of M.Tech Thesis  
**Prof. Abhirup Datta**

-----  
**Kundan Sahu** has successfully given his M.Tech Oral Examination held on 25<sup>th</sup> April, 2024

*S. Das*

Programme Coordinator, M.Tech

Date: - 24/05/2024

*S. Das*

Convener, DPGC

Date: - 24/05/2024

*Abhirup Datta*

Thesis Supervisor

Date: - 24/05/2024

*Abhirup Datta*

Head of Discipline

Date: - 24/05/2024

# ACKNOWLEDGEMENT

I want to express my sincere gratitude to my thesis advisor, Prof. Abhirup Datta, for his unwavering support and guidance throughout this research project. I acknowledge the assistance provided by PhD. scholar Harsha Avinash Tanti and my labmates throughout this project. Their insightful comments and constructive criticism helped me to shape and refine my ideas, and their dedication and commitment to this project have been invaluable. I would also like to thank the faculty and staff at DASSE, especially the members of RF Lab, for their encouragement and support during my time as a graduate student. I would like to acknowledge the contributions of my colleagues and classmates Sudhanshu, Mohit, Sheshank, and Tiasha and all my friends in campus, who have provided me with friendship, support, and encouragement throughout my studies. Their camaraderie and collaboration have been a source of inspiration and motivation.

Thank you all for your support and encouragement.

# ABSTRACT

CubeSats are tiny space exploration vessels with a lower cost than most satellites in history. Studies on this technology are flourishing, as evidenced by the doubling of published research between initial exploration and final projects. These versatile mini-satellites fulfill diverse missions while adhering to a standardized, compact design.

Inspired by Phase I & II of the Space Electric and Magnetic Sensor (SEAMS) mission, which is aimed at performing an RFI survey and testing out interferometric principles respectively, we propose a mission wherein we will try to observe an RFI scenario and perform an interferometer using a tethered system in this work. With this mission, we can get an insight into what other factors may affect the interferometer experiment of SEAMS phase II. The proposed tethered CubeSat system will comprise a 2U and 1U CubeSat and will be launched as a combined 3U payload into Low Earth Orbit (LEO). Upon reaching LEO, the 1U CubeSat will autonomously deploy from the 3U CubeSat.

The primary objective of this study is to validate the electronic functionality and effectiveness of a tethered CubeSat system for performing astronomical observations using radio interferometry. In this study, I present FEA analysis of the CubeSat structure, Two-Element interferometer configuration, designing of the backend, and processing to observe interferometric fringes.

## LIST OF PUBLICATIONS

- **K. Sahu**, B. R. P. Tej, K. S. Shekhar and A. Datta, “*Structural and Thermal Analysis of a Modular 1U CubeSat for RFI Survey on LEO orbit*” 2023 8th International Conference on Computers and Devices for Communication (CODEC), Kolkata, India, 2023, pp. 1-2, doi: 10.1109/CODEC60112.2023.10466039.
- H. A. Tanti, **K. Sahu**, A. Datta and A. K. Pradhan, “*Tri-axial Patch antenna array configuration for Direction of Arrival (DoA) application*” 2023 8th International Conference on Computers and Devices for Communication (CODEC), Kolkata, India, 2023, pp. 1-2, doi: 10.1109/CODEC60112.2023.10465763.

# Contents

<b>1</b>	<b>Introduction</b>	<b>1</b>
1.1	CubeSat Background . . . . .	2
1.1.1	India’s CubeSat Missions . . . . .	2
1.2	Tethers in space . . . . .	4
1.2.1	History of Tether . . . . .	4
1.2.2	Application and Missions . . . . .	5
1.2.3	Role of Tether Materials . . . . .	5
1.3	Radio Frequency Interference . . . . .	7
1.3.1	Classification of RFI . . . . .	7
1.3.2	Types of Noise . . . . .	8
1.3.3	Radio Frequency Interference Detection and Mitigation . . . . .	8
1.4	Radio Interferometer . . . . .	9
1.4.1	Quantifying radiation . . . . .	9
1.4.2	Radio Telescope: . . . . .	11
1.4.3	Observations using Single dish Radio Telescope and its Limitations . . . . .	13
1.4.4	Need of interferometer . . . . .	15
<b>2</b>	<b>Motivation and Objective</b>	<b>17</b>
2.1	Motivation . . . . .	17
2.2	Mission Sequence . . . . .	17
2.3	Objectives: . . . . .	18
<b>3</b>	<b>Proposed Payload</b>	<b>19</b>
3.1	Subsystems: . . . . .	19
3.1.1	CubeSat Architecture: . . . . .	19
3.1.2	Deployment Mechanism of tethered system: . . . . .	19
3.1.3	Patch Antennas: . . . . .	20
3.1.4	Backend Processing Unit: . . . . .	21
3.1.5	On-Board Computer (OBC): . . . . .	23
3.1.6	Telemetry, Tracking and Command Handling . . . . .	25
3.1.7	Electric Power System . . . . .	27
3.1.8	Attitude Determination and Control System . . . . .	28

<b>4</b>	<b>Design and Development</b>	<b>31</b>
4.1	CubeSat Chassis . . . . .	31
4.1.1	Design & Modelling of 1U structure . . . . .	33
4.1.2	Result . . . . .	33
4.1.3	Design & Modelling of 2U structure . . . . .	35
4.1.4	Result . . . . .	35
4.1.5	3U Modular Structure . . . . .	38
4.2	Antenna Design . . . . .	43
4.2.1	Design . . . . .	43
4.2.2	Result . . . . .	44
<b>5</b>	<b>The RFRI Instrument</b>	<b>46</b>
5.1	RFI meter . . . . .	46
5.1.1	Block Diagram: . . . . .	46
5.2	Radio Interferometer: . . . . .	49
5.2.1	Block Diagram: . . . . .	49
5.2.2	Phase Calibration . . . . .	51
5.2.3	Backend Testing . . . . .	51
5.2.4	On field test with patch antenna . . . . .	55
<b>6</b>	<b>Conclusion and Future Scope</b>	<b>57</b>
6.1	Conclusion . . . . .	57
6.2	Future Scope . . . . .	57

## BIBLIOGRAPHY

# List of Figures

1.1	CubeSat Family [1] . . . . .	3
1.2	(a) STUDSAT (b) Jugnu (c) Swayam (d) Pratham . . . . .	4
1.3	Basic tether configuration . . . . .	5
1.4	Fraction of the total luminosity emitted by the source [2] . . . . .	10
1.5	Primary parabolic reflector . . . . .	11
1.6	Parts of Radiation Pattern [3] . . . . .	12
1.7	Parts of Radio telescope [4] . . . . .	13
1.8	Two element interferometer [2] . . . . .	16
2.1	Mission sequence . . . . .	18
3.1	OEDIPUS-A payload configuration [5] . . . . .	20
3.2	SEDS Functional Diagram [6] . . . . .	21
3.3	LimeSDR-USB Development Board [7] . . . . .	22
3.4	GRC Window . . . . .	24
3.5	Telemetry, Tracking and Command System [8] . . . . .	26
3.6	Basic EPS Block . . . . .	28
3.7	Block diagram of ADCS System [9] . . . . .	29
4.1	Heat Flux Sources for a CubeSat [10] . . . . .	32
4.2	CAD Model . . . . .	33
4.3	Structural Simulation . . . . .	34
4.4	Thermal Simulation . . . . .	34
4.5	Modular 2U designs . . . . .	36
4.6	Total deformation of the two modular structures under 16g . . . . .	36
4.7	Total heat flux of the two modular structures . . . . .	36
4.8	Harmonic response graph of both cubesat structure . . . . .	37
4.9	(a) Modified 1U structure (b) Modified 2U structure (c) Combined 3U structure . . . . .	39
4.10	(a) Total Deformation (b) Directional Deformation (c) Equivalent (von Mises) stress distribution, subject to static loads of 11 g in the “z” axis and 6 g in both for “x” and “y” . . . . .	40
4.11	(a) Total Deformation (b) Directional Deformation (c) Equivalent (von Mises) stress distribution, subject to static loads of 16g in x,y and z direction simultaneously . . . . .	41
4.12	Thermal Simulation . . . . .	42

4.13	(a) Schematic of the inset feed microstrip patch antenna (b) Fabricated inset feed microstrip patch antenna . . . . .	43
4.14	(a) $S_{11}$ (b) 2D radiation pattern of simulated and measured patch antenna	44
5.1	RFIM block diagram . . . . .	46
5.2	RFIM Lab Setup . . . . .	47
5.3	(a) Data taken inside Anechoic Chamber (b) Data taken outside Anechoic Chamber . . . . .	47
5.4	GNU blocks for RFIM . . . . .	48
5.5	Basic Interferometer block diagram . . . . .	49
5.6	GNU flow diagram . . . . .	49
5.7	Graphical depiction of polyphase filtering [11] . . . . .	50
5.8	GNU blocks for Interferometer . . . . .	52
5.9	(a) Interferometer's baseline geometry, with plane waves arriving vertically (b) Phase vs Amplitude graph . . . . .	53
5.10	Backend Components: SDR and SBC Integration . . . . .	53
5.11	Setup of a Two-Element Interferometer with Horn Antennas . . . . .	53
5.12	(a) 2D plot of data (b) Fringe pattern plot . . . . .	54
5.13	Test setup using patch housed by 3D printed CubeSat structure . . . . .	55
5.14	Setup of a Two-Element Interferometer with Patch antennas . . . . .	55
5.15	2D plot of patch data . . . . .	56
5.16	1D plot of patch data . . . . .	56

# Chapter 1

## Introduction

Radio Interferometry is a powerful technique for astronomical observation that combines the signals from multiple telescopes to provide enhanced resolution and sensitivity, allowing astronomers to probe the universe with unprecedented details. However, terrestrial interferometry encounters limitations that hinder its full potential. Earth-based interferometers are susceptible to atmospheric disturbances, such as turbulence and absorption, which degrade the quality of observations, particularly at longer wavelengths. Additionally, the precise alignment and synchronization of widely spaced telescopes also pose significant challenges [12, 13].

To overcome these limitations, space based interferometry missions have emerged as promising alternatives. Operating above the distorting effects of Earth's atmosphere, space interferometers offer unparalleled observing conditions for capturing high-resolution astronomical data [14]. A number of interferometric space missions have therefore been proposed. Some of these missions include Orbiting stellar interferometer for astrometry and imaging [15], Darwin – The Infrared Space Interferometry Mission [16], Sub-millimeter Probe of the Evolution of Cosmic Structure (SPECS) [17], AERO & VISTA: Demonstrating HF Radio Interferometry with Vector Sensors [18], and FARSIDE: A Low Radio Frequency Interferometric Array on the Lunar Farside [19].

CubeSats, with their compact size, low cost, and modular design, present an ideal platform for implementing tethered interferometry in space. These miniature satellites can be easily deployed and interconnected via tethers to form a stable interferometer system [20]. Some of the Cubesat tethered missions include Multi-Application Survivable Tether(MAST) [21], Space Tethered Autonomous Robotic Satellite(STARS) [22] and AeroCube-3 [23].

Despite these advantages, space interferometers face their own set of challenges. Ensuring precise alignment, maneuvering, and synchronized motion among multiple spacecraft poses a significant challenge in formation flying missions. This complexity escalates mission costs and intricacy [24]. A Tethered interferometer system as an intermediary step will provide insight into the challenges of a space-based interferometer. This approach ensures there is proper synchronization between the elements of the interferometer, mitigating one of the major challenges associated with communication and signal delays. The tether can also be deployed or retracted to vary the baseline for interferometric observations. A similar performance can also be achieved

by tethering smaller satellites such as CubeSats together to provide a cost-effective alternative to large, monolithic satellites [25, 26].

Due to the potential of interferometry and the need for novel solutions in space exploration, we study and develop a tethered CubeSat system that aims to demonstrate the principles of interferometry within the context of a tethered CubeSat system deployed in low Earth orbit (LEO).

Drawing inspiration from Phase I and II of the Space Electric and Magnetic Sensor (SEAMS) mission [27], which were designed to conduct a Radio Frequency Interference (RFI) survey and explore interferometric principles, respectively, this paper proposes a mission to investigate RFI scenarios and implement an interferometer using a tethered system. With this mission, we can get insight about what other factors may affect the interferometer experiment of SEAMS phase II and other space-based interferometer missions.

## 1.1 CubeSat Background

CubeSats, a category of nanosatellites, adhere to a standardized size and form factor. The conventional CubeSat dimensions are denoted as “1U” or one unit,” measuring 100 mm x 100 mm x 100 mm, and can be scaled to larger sizes, including 1.5U, 2U, 3U, 6U, and even 12U (Fig. 1.1). Originating in 1999 through collaborative efforts by California Polytechnic State University at San Luis Obispo (Cal Poly) and Stanford University, CubeSats were initially designed to serve as a versatile platform for educational purposes and space exploration. Over time, the development of CubeSats has evolved into a distinct industry, with active collaboration among government entities, industries, and academic institutions, resulting in continually expanding capabilities. CubeSats have emerged as a cost-effective solution for conducting scientific investigations, showcasing new technology, and implementing advanced mission concepts, such as constellations, swarms, and modular systems. Table 1.1 shows the typical maximum mass for each U configuration [1].

U Configuration	Mass (KG)
1U	2.00
1.5U	3.00
2U	4.00
3U	6.00
6U	12.00
12U	14.00

Table 1.1: CubeSat Mass Specifications [1]

### 1.1.1 India’s CubeSat Missions

Below are some CubeSat missions by India [28]:

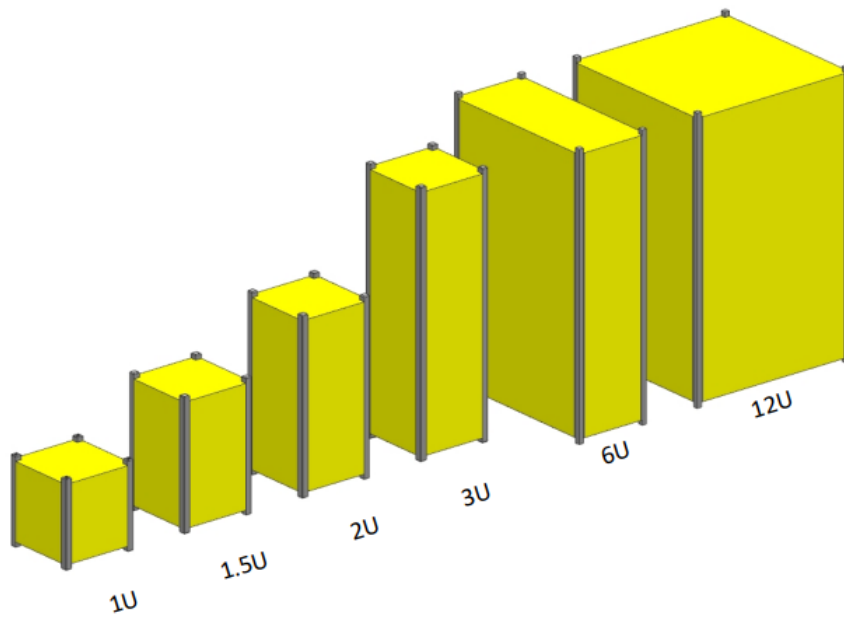


Figure 1.1: CubeSat Family [1]

### **STUDSAT**

STUDSAT is a 1U picosatellite successfully launched into a Sun-synchronous orbit on July 12, 2010, from the Satish Dhawan Space Centre. The mission's objective was for students to gain practical experience in the design, manufacture, and implementation of a low-cost space mission.

### **Jugnu**

Jugnu is a 3U CubeSat, which was used for remote sensing and technology demonstration. It was operated by the Indian Institute of Technology Kanpur. Jugnu was launched on 12 October 2011 into low Earth orbit by PSLV-CA C18.

### **Swayam**

Swayam is a small satellite, a CubeSat of 1U size, created by undergraduate students from the College of Engineering, Pune. It was sent into space by ISRO on June 22, 2016, sharing a launch with Cartosat-2C aboard the Polar Satellite Launch Vehicle C-34 from the Satish Dhawan Space Center in Sriharikota, India.

### **Pratham**

Pratham is a 1U satellite designed for ionospheric research in India. It was operated by the Indian Institute of Technology Bombay as part of the Student Satellite Initiative. Its main goal is electron counting in Earth's ionosphere. The cube-shaped Pratham weighs around 10.15 kilograms and measures 30 centimeters on each side. It was

effectively launched on September 26, 2016, from Satish Dhawan Space Centre in Sriharikota, Andhra Pradesh, alongside seven other satellites on PSLV C-35.

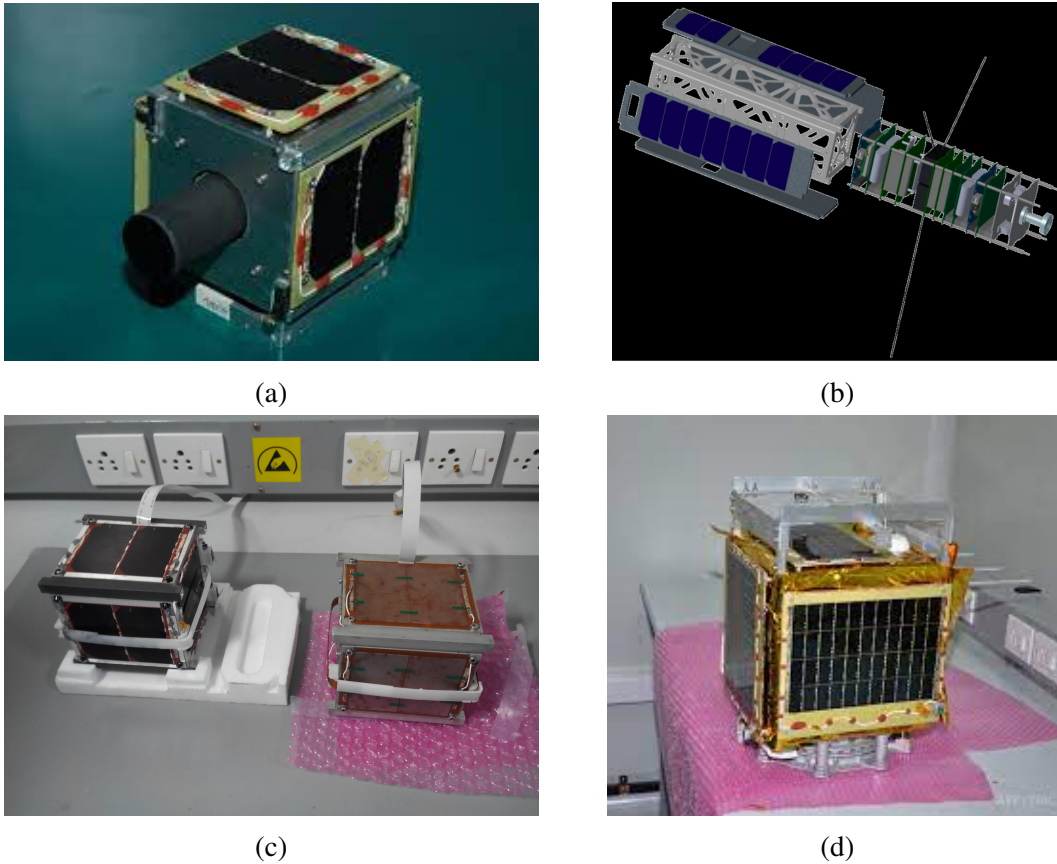


Figure 1.2: (a) STUDSAT (b) Jugnu (c) Swayam (d) Pratham

## 1.2 Tethers in space

The concept of space tethers dates back to 1895, and research on them, particularly their dynamics and control (essential aspects for successful use), has grown rapidly ever since. Over the past century, a number of space tether missions have been flown, primarily to test and learn more about these tethers in a real space environment. [20].

### 1.2.1 History of Tether

In 1895, Konstantin Tsiolkovsky envisioned a giant tower reaching space, a precursor to the modern concept. The idea evolved in 1960 when Yuri Artsutanov proposed a cable lowered from a geostationary satellite. This concept was reinvented by others as the “Skyhook” but material limitations were a hurdle. Jerome Pearson addressed this in 1975 with a tapered cable design. Challenges remained. Building the structure would require immense resources. Despite this, the space elevator captured the public imagination, appearing in Arthur C. Clarke’s 1979 novel “The Fountains of Paradise”.

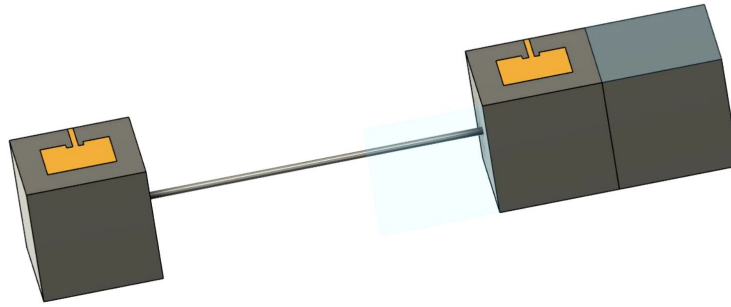


Figure 1.3: Basic tether configuration

Research continued through the 1980s, focusing on alternative designs and control methods for space tethers used for various purposes. These tethers held promise for applications like deploying satellites and deorbiting spacecraft. While a true space elevator remains out of reach, research on space tethers for various applications paves the way for future advancements, keeping the dream alive.

### 1.2.2 Application and Missions

Over the past years, advancements in space tech have led to a surge in tethered satellite missions. These missions have explored a wide range of applications, including Station Tethered Express Payload System (STEPS), multiprobe for atmospheric studies, gravity wave detection, Earth-Moon tether transport system, Space Elevator, electrodynamic power/thrust generation, comet/asteroid sample return, tethered lunar satellite for remote sensing, cosmic dust collection etc. [29]. Some of the recent missions listed in the table 1.2

### 1.2.3 Role of Tether Materials

While tether design depends on its specific use, some key properties are universal. Ideal tethers, for both performance and affordability, would be made from strong or highly conductive materials that are also lightweight. Since space debris and micrometeoroids pose a threat, designers must consider adding a protective coating to shield the tether from factors like ultraviolet radiation and atomic oxygen. Ideal tether materials must possess a remarkable combination of properties:

- **High Strength-to-Weight Ratio:** The tether needs to be incredibly strong to withstand the immense tension forces acting upon it during operation. Yet, it must also be lightweight to minimize the launch mass.
- **High Stiffness:** The tether should exhibit minimal stretching to maintain its shape and perform its intended function effectively.
- **Durability:** Space tethers endure a harsh environment with extreme temperatures, radiation exposure, and the potential for micrometeoroid impacts. The chosen material must be resistant to degradation over extended periods.

Mission Name	Nation	Type	Launch Date	Status	Mission Description
MAST	US	3U	2007-04-17	Was semi-operational	Three tethered CubeSats with 1 km tether and middle one will crawl up and down the tether
STARS 1	Japan	3.8 kg	2009-01-23	Reentered, Was operational	Two satellite system connected with 5m tether
AeroCube-3	US	1U	2009-05-19	Reentered, Was operational	Attached to the upper stage of its carrier rocket by means of a 61m tether
STARS-C	Japan	1U	2016-12-09	Reentered, Operational	Demonstration of tethered satellites for future space elevator
STARS-Me A Mother	Japan	1U	2018-09-22	Reentered, Was operational	Connected by tether to research technologies for space elevator
STARS-EC A, B, C	Japan	1U	2021-02-20	Reentered, Operational	Elevator lifting of about 22m experiment with 3 satellites connected by tethers

Table 1.2: Recent Space Tether Missions [21] [22] [30]

The selection of tether materials, both metal and non-metal, follows strict guidelines set by MSFC-STD-506. However, depending on the specific needs of the tether system, these guidelines might be adjusted to optimize functionality and reliability. Ideally, materials with established acceptance ratings according to the MSFC-HDBK-527 database will be chosen. In cases where material falls outside the acceptable range of MSFC-STD-506, a special approval process outlined in MSFC-PROC-1301 must be followed. Additional considerations are needed for tethers containing electrical conductors to prevent unintended electrical discharges [31].

**Common Tether Materials:**

- **Spectra:** A high-strength polyethylene fiber known for its impressive strength-to-weight ratio.

- **Kevlar:** An aramid fiber prized for its high tensile strength and modulus (stiffness).
- **Dyneema:** An ultra-high-molecular-weight polyethylene (UHMWPE) fiber offering excellent strength and low weight.
- **Carbon Nanotubes (CNTs):** While still under development for space tethers, CNTs hold immense promise due to their exceptional strength, stiffness, and low density.

Material	Density(g/cc)	Tensile Strength(MPa)	Elasticity Modulus(GPa)
Spectra 900	0.97	2590	117
Kevlar 49	1.44	3600	112.4
Dyneema	0.98	3900	132
Carbon Nanotubes (CNTs)	1.4	48000	154

Table 1.3: Comparison table of material

## 1.3 Radio Frequency Interference

Radio Frequency Interference (RFI) refers to the presence of unwanted signals or electromagnetic emissions in the radio frequency spectrum, disrupting the normal operation of communication systems, radar, or other electronic devices. RFI can occur when signals from one source interfere with the reception or transmission of signals from another source. It is a common challenge in various applications, including radio astronomy, wireless communication, satellite communications, and navigation systems.

It originates from both man-made sources, such as electronic devices and industrial equipment, and natural sources like lightning and cosmic phenomena. RFI has widespread effects, impacting communication systems by causing signal degradation, data rate reduction, and increased error rates. In radio astronomy, RFI poses a significant challenge, distorting or masking celestial signals and compromising the accuracy of observations.

Radio Frequency Interference (RFI) includes unwanted radio signals that radio telescopes pick up from human related activities or things happening on Earth. This interference can come from inside the telescope or outside sources like electronic devices, networks, or natural sources such as the Sun or Earth. Detecting RFI is crucial for preparing radio astronomy data.

### 1.3.1 Classification of RFI

Intentional and inadvertent radio frequency interference (RFI) fall into two primary kinds. Deliberate attempts to send signals in a certain frequency band, frequently for broadcasting or communication, result in intentional RFI. Television and radio stations are two examples. Conversely, inadvertent radio frequency interference (RFI) is undesired interference that arises from different electronic equipment inadvertently

sending out signals, interfering with adjacent communication networks. Electronic devices, machinery, and electrical equipment are common sources of inadvertent RFI.

Apart from deliberate and inadvertent radiofrequency interference, interference may also be classified according to how it affects communication networks. Broadband interference covers a larger spectrum than narrowband interference, which only impacts a certain frequency range. Determining and categorizing RFI is essential to creating practical mitigation solutions.

### 1.3.2 Types of Noise

- **Thermal Noise:** Arises due to the random motion of electrons in a conductor and increases with temperature.
- **Shot Noise:** Occurs in electronic devices and is associated with the discrete nature of the electric charge.
- **White Noise:** Characterized by a flat frequency spectrum, where all frequencies have equal intensity.
- **Gaussian Noise:** Follows a Gaussian or normal distribution, often seen as random fluctuations in signals.
- **Quantization Noise:** Results from the approximation of continuous signals into discrete digital values.
- **Cross-Talk:** Signal interference between adjacent channels or conductors.
- **Intermodulation Noise:** Arises when non-linearities in a system cause signals to mix and produce unwanted frequencies.
- **Environmental Noise:** Includes external factors like electromagnetic interference (EMI), radio-frequency interference (RFI), and other external disturbances.

### 1.3.3 Radio Frequency Interference Detection and Mitigation

RFI includes unwanted signals like spurious signals and harmonics from lower frequency bands. It also involves spread-spectrum signals overlapping with the intended frequency band or emissions that pre-detection filters can't fully reject. RFI can mess up the accuracy of measurements, especially in crowded areas. Detecting and dealing with RFI in microwave radiometry involves different methods to prevent these unwanted signals from causing problems in data collection [32].

- **Time Domain:** In time-domain methods, signal samples displaying power peaks exceeding a predefined factor of the anticipated variance are typically removed ("eliminated"). Nevertheless, because the detected power represents an average of the instantaneous power, RFI peaks with durations shorter than the integration time might go unnoticed.

- **Frequency Domain:** Similar to time-domain techniques, the detected power is an average over a specific bandwidth. Consequently, power peaks of Radio Frequency Interference (RFI) that are narrower than the resolution bandwidth may go unnoticed due to this “blurring” effect.

Spectrogram techniques, which combine time- and frequency-domain signal analysis, use extended data sequences for detailed resolution in both dimensions. High-power time-frequency bins are identified through image processing, and clusters of such bins are detected, leading to the removal of anomalous high-power instances. In all these approaches, the remaining signal samples, subbands, or time-frequency bins are used to estimate the signal power, appropriately adjusted for accuracy.

## 1.4 Radio Interferometer

In astronomy, the ability to image celestial objects is paramount for studying their properties and understanding the underlying physical processes. However, for faint radio emissions, traditional imaging techniques based on the particle nature of light (e.g., photoelectric effect) are rendered ineffective. This inherent limitation necessitates alternative approaches in radio astronomy. Radio interferometry emerges as a powerful tool, exploiting the wave nature of electromagnetic radiation, particularly the phenomena of interference and diffraction, to overcome the substantial challenge of “imaging” faint radio signals. Image is basically a spatial distribution of intensity. By analyzing the interference patterns generated by electric fields, originating from electromagnetic emissions from a celestial object, scientists can infer its intensity distribution, essentially creating a “radio image.”

### 1.4.1 Quantifying radiation

One quantitative measure that astronomers can make when they observe a light source is the amount of radiation that is received. To gain insights into the physical characteristics of an object, astronomers rely upon the amount of radiation emitted by them. The amount of emission is quantified by [2] :

- **Luminosity(L):** The power or the rate of emission of energy is luminosity. Its unit is  $J s^{-1}$  or W. However, it cannot be directly measured because a significant portion of the radiation is emitted in directions away from the telescope and most of the information gets lost.
- **Flux(F):** the amount of light energy per unit time per unit area. The units of flux are  $J s^{-1} m^{-2}$  or  $W m^{-2}$  (SI) and  $ergs s^{-1} cm^{-2}$  (cgs). The amount of light (flux) received from a celestial object is directly linked to its intrinsic brightness, known as luminosity. An object’s luminosity is estimated by calculating the fraction of its total emitted radiation that reaches the telescope. Let, telescope with effective area ‘ $A_{eff}$ ’ is at a distance ‘d’ from the source, having luminosity

L. Then ,

$$F = L/4\pi d^2 \quad (1.1)$$

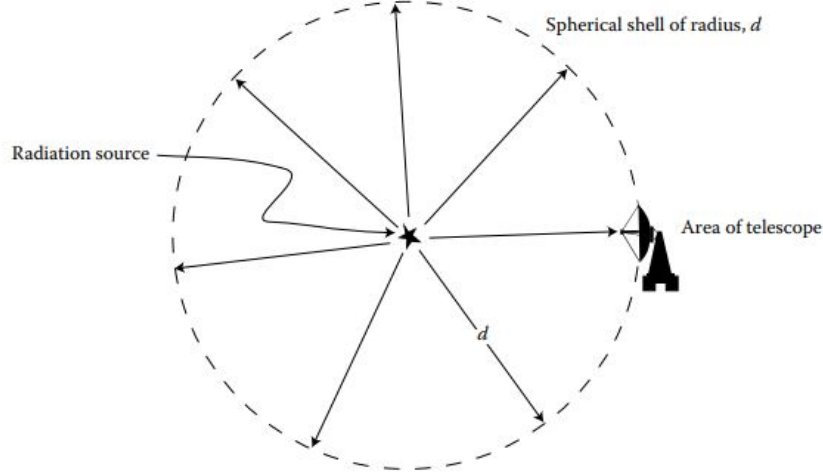


Figure 1.4: Fraction of the total luminosity emitted by the source [2]

Power(P) detected by the telescope is

$$P = L \frac{A_{eff}}{4\pi d^2} = F A_{eff} \quad (1.2)$$

Similarly, it is also not a measurable quantity as the radiation emitted at all frequencies over the entire E.M. spectrum is not captured by the telescope.

- **Flux Density( $F_\nu$ ):** The detected flux per frequency bandwidth( $\Delta\nu$ ) in the observed spectral range. Its unit is  $Wm^{-2}Hz^{-1}$  .

$$F_\nu = \frac{P}{\Delta\nu} \quad (1.3)$$

It is a measurable quantity that can be directly obtained and is consistent among all observers, irrespective of the telescope employed.

The power received by a telescope is directly proportional to the flux density of the observed source and is given by

$$P = F_\nu A_{eff} \Delta\nu \quad (1.4)$$

In the domain of radio astronomy, a significant unit of measurement is,

$$1jansky(Jy) = 10^{-26}Wm^{-2}Hz^{-1} \quad (1.5)$$

- **Intensity( $I_\nu$ ):** It represents the amount of flux per unit solid angle ( $\Omega$ ). It is also known as surface brightness. Unit is  $Wm^{-2}Hz^{-1}sr^{-1}$ . It is independent of distance but gives an idea about the direction of photons.

$$I_\nu = \frac{F_\nu}{\Omega} \quad (1.6)$$

## 1.4.2 Radio Telescope:

Radio telescopes are the ‘lenses’ in radio astronomy. A typical radio telescope consists of a primary reflector(or dish), feed, transmission line, and receiver.

### Primary Reflector:

Most of the dishes of radio telescopes are parabolic reflectors (Fig.1.7). Radio signals are weak in nature. So, for detecting faint sources, focusing multiple radio waves toward the detecting element(antenna) is required. The dishes are responsible for focusing on the incident E.M. waves in a particular plane are the reflectors. Due to this function, they are shaped as a parabola. The amount of radiation that can be focused depends on the effective area of the dish ( $A_{eff}$ ). Another important function of a reflector is to provide directivity, i.e. the capability to distinguish the emission from celestial objects at various angular positions. When using a single radio telescope to make a map the directivity determines the resolution in the map.

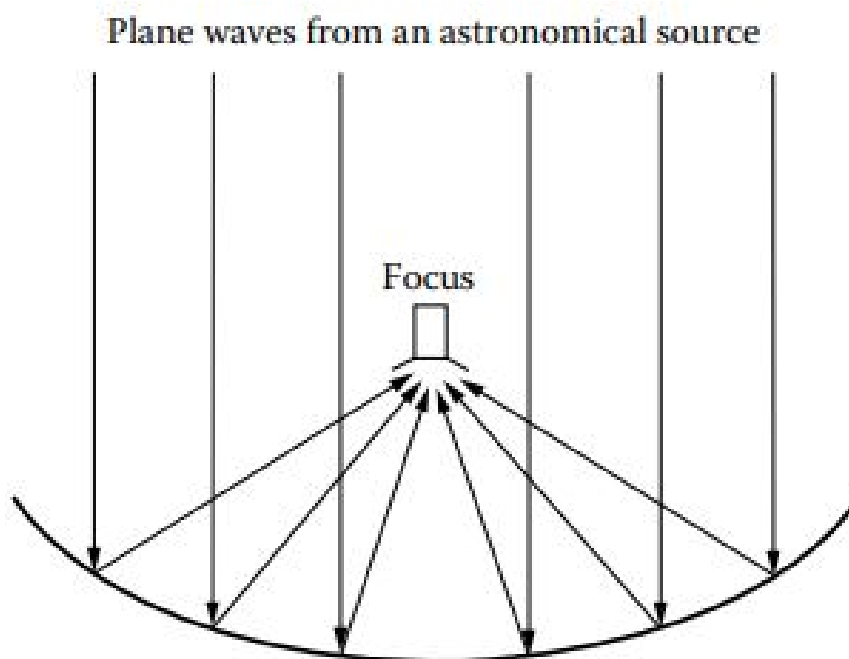


Figure 1.5: Primary parabolic reflector

### Feed:

The primary component to sense an E.M. wave is an antenna. It is responsible for the conversion of an E.M. wave into an electric signal and vice-versa. In radio astronomy, it serves as the “lens.” An important characteristic of antennas is that the direction of reception and that for transmission of signals remain the same. However, each antenna has a distinct radiation pattern. The beam of an antenna consists of different parts:

- **Primary Lobe:** This is the region of the beam where the highest amount of energy is emitted.
- **Secondary or Back Lobe:** It lies exactly opposite to the primary lobe. A significant portion of energy is either wasted (in transmission mode) or, conversely, senses undesired signals (in receiving mode).
- **Side Lobe:** When radiation is dispersed laterally, it gives rise to side lobes or minor lobes. In this scenario, power is either wasted (in transmission mode) or, conversely, catches undesired signals (in receiving mode).

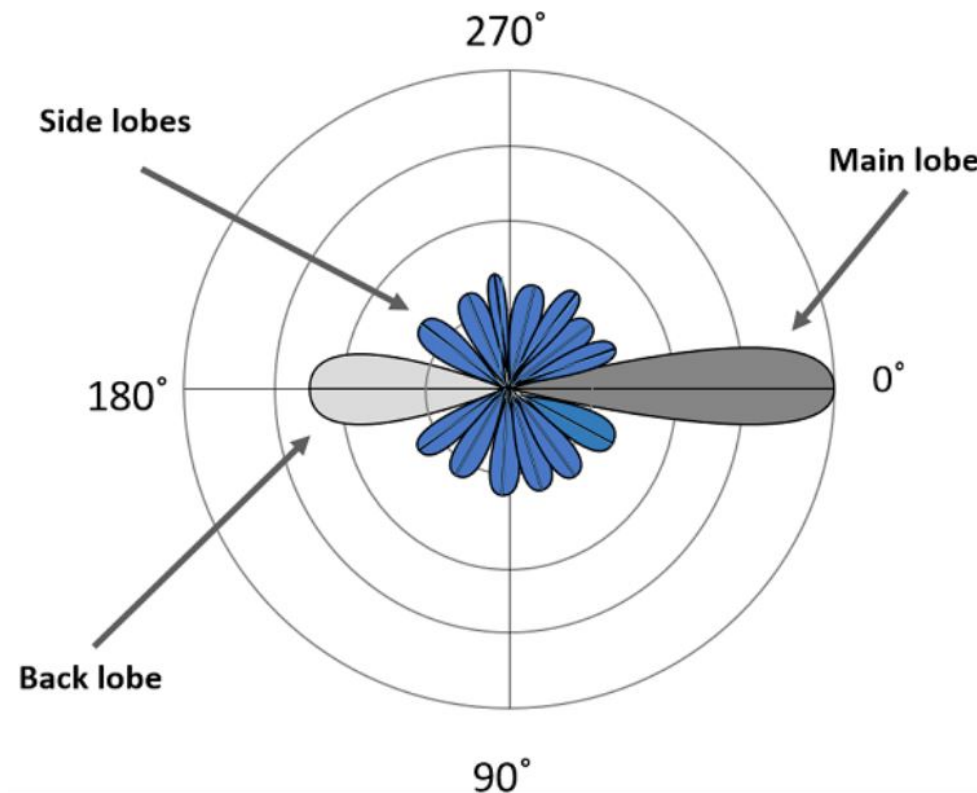


Figure 1.6: Parts of Radiation Pattern [3]

The area of the sky an antenna can map depends on the primary beam. So, the choice of antenna for performing interferometry is crucial. Moreover, these are also sensitive to the polarization of the signals.

#### Receivers:

The radio telescope receiver has two main purposes: it determines the range of frequencies it will gather power from, and it creates a signal that represents the collected power, which can then be recorded. It comprises of transmission lines, filters, amplifiers, and signal detectors (Fig. 1.7).

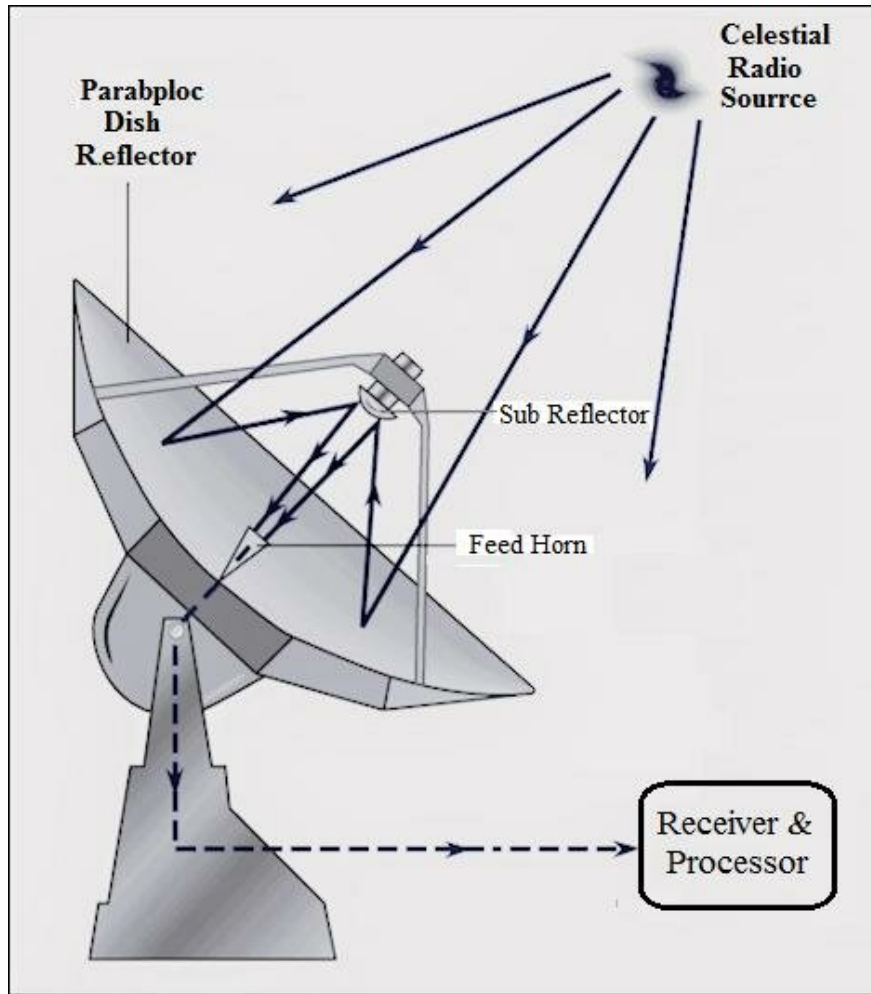


Figure 1.7: Parts of Radio telescope [4]

### 1.4.3 Observations using Single dish Radio Telescope and its Limitations

#### Method

From the power detected by an antenna in a radio telescope, it is possible to obtain the source's intensity distribution:

$$P = F_{\nu} A_{\text{eff}} \Delta\nu \quad (1.7)$$

where  $P$  is the power detected by the telescope with the effective area ( $A_{\text{eff}}$ ),  $F_{\nu}$  is the flux density of the source, and  $\Delta\nu$  is the bandwidth over which observation is done.

The power can be described by its equivalent temperature, antenna temperature ( $T_A$ ), related by:

$$V = \alpha G k \Delta\nu (T_A) \quad (1.8)$$

where  $V$  is the voltage measured by the detector,  $\alpha$  is the responsivity of the detector,  $G$  is the gain of the receiver, and  $k$  is Boltzmann's constant.

However, in reality, noise also gets embedded into the signal of interest:

$$V = \alpha G k \Delta \nu (T_A + T_{\text{sys}}) \quad (1.9)$$

where  $T_{\text{sys}}$  quantifies all the unwanted power.

To obtain  $T_A$ , observations are taken twice, once with the source ( $V_{\text{on}}$ ) and another time without the source ( $V_{\text{off}}$ ), known as switching observations:

$$V_{\text{on}} - V_{\text{off}} = \alpha G k \Delta \nu T_A \quad (1.10)$$

This technique allows for calibration to obtain  $T_A$ .

$T_A$  at position  $(\theta_0, \phi_0)$  is related by source intensity ( $I_\nu$ ):

$$T_A = \frac{A_{\text{eff}}}{2k} \int_{\text{sky}} I_\nu(\theta, \phi) P_{\text{bm}}(\theta - \theta_0, \phi - \phi_0) d\Omega \quad (1.11)$$

where  $P_{\text{bm}}(\theta, \phi)$  is the antenna beam.

## Generating Maps and Limitations

To generate a map using a single-dish radio telescope, the telescope must be directed toward a specific celestial direction, where a switched observation is conducted. The measured antenna temperature is recorded. Subsequently, the telescope is repositioned to a new location, and the entire process is iterated until the desired region of the sky is adequately covered. By converting the antenna temperatures from all these positions, a comprehensive map of the radio source can be derived.

### Limitations

Single-dish radio telescopes, while valuable for certain observations, have limitations that can affect their performance and capabilities:

- **Spatial Resolution:** Single-dish telescopes typically have a lower spatial resolution ( $\lambda/D$ ,  $D$  = diameter of the telescope aperture) compared to interferometers.
- **Confusion in Crowded Fields:** In regions of the sky with numerous radio sources, a single-dish telescope may encounter confusion, making it challenging to distinguish between overlapping signals from different sources.
- **Sensitivity to Extended Emission:** Single-dish telescopes are more sensitive to extended sources but may struggle to provide detailed information on compact sources or features with angular sizes smaller than the telescope's beam.
- **Limited Spectral Information:** Single-dish telescopes may have limitations in obtaining detailed spectral information. Spectral line studies can be more effectively carried out by interferometers with multiple baselines.

- **Observational Time Constraints:** To cover large areas of the sky, single-dish telescopes may require significant observational time. This limitation becomes apparent when compared to interferometers that can simultaneously observe multiple baselines. Moreover, during switched observations, the ‘switching’ needs to be done quite rapidly.
- **Difficulty in Identifying Source Components:** Identifying and separating multiple components within a single observation can be more complex with single-dish telescopes compared to interferometers, which can provide better spatial discrimination.

Despite these limitations, single-dish radio telescopes remain essential tools in radio astronomy, especially for surveys, monitoring large-scale structures, and detecting extended emissions. They complement the capabilities of interferometers, and the choice between the two depends on the specific scientific goals of the observation.

#### 1.4.4 Need of interferometer

The idea that the resolution of optical instruments is limited due to the wave nature of light is familiar to students of optics and is embodied in Rayleigh’s criterion which states that the angular resolution of a telescope/microscope is ultimately diffraction-limited and is given by

$$\theta \sim \frac{\lambda}{D} \quad (1.12)$$

where  $D$  is some measure of the aperture size. Unlike optical telescopes, radio telescopes struggle with seeing fine details due to long radio wavelengths. Bigger telescopes don’t solve this problem. To get sharper images, astronomers use shorter wavelengths (cm/mm), but this limits what they can study. Building a giant radio telescope isn’t feasible. Here’s where aperture synthesis comes in. Like teamwork, it combines data from multiple smaller telescopes, creating a virtual giant with superior resolution. Similar to the double-slit experiment, this technique unlocks incredible detail, allowing astronomers to see the universe with unprecedented clarity.

Fig.1.8 depicts an interferometer, composed of two antennas separated by a distance  $b$  (baseline), that receives signals from a radio source at an angle  $\theta$  relative to the zenith. Therefore, for resolution of the interferometer, equation 1.12 can be rewritten as

$$\theta \sim \frac{\lambda}{b} \quad (1.13)$$

where  $b$  is the baseline equivalent to  $D$ . Consider the source as a point. This source has a certain flux density  $F_n$  and is positioned in the plane formed by the antennas and the baseline zenith, making an angle  $\theta$  with the zenith.

When an electromagnetic wave reaches and enters the antennas, parts of the wavefront enter each antenna with a slight delay due to the different distances they must travel. This delay causes a phase difference between the signals received by the antennas. The delay ( $\tau$ ) can be calculated using trigonometry as

$$\tau = \frac{\Delta s}{c} = \frac{b}{c} \sin \theta \quad (1.14)$$

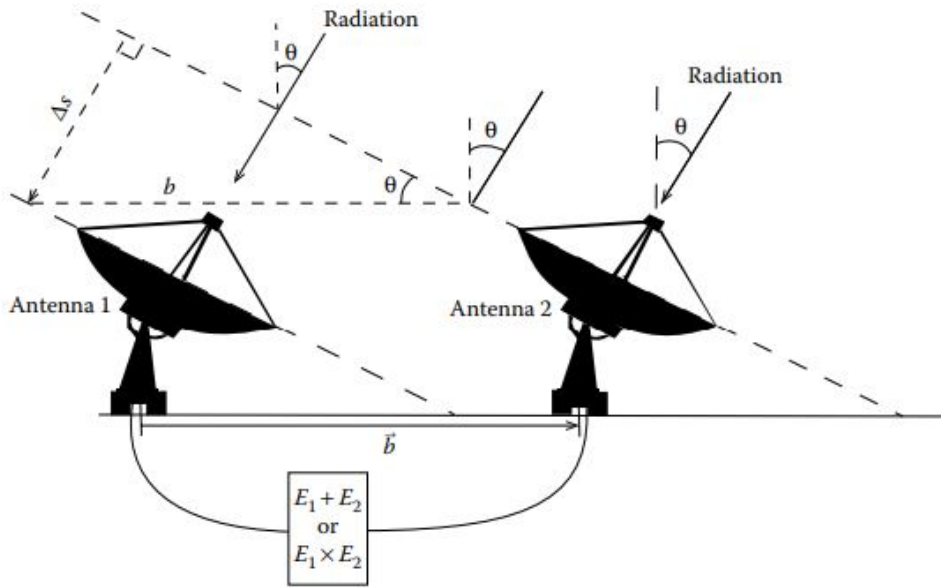


Figure 1.8: Two element interferometer [2]

, where  $c$  is the speed of light.

This phase difference leads to differences in the electric fields received by the antennas, given by

$$E_1 = E_0 \cos(2\pi\nu t) \quad (1.15)$$

and

$$E_2 = E_0 \cos(2\pi\nu t + \Delta\Phi) \quad (1.16)$$

, where  $t$  is the time,  $\nu$  is the frequency,  $E_0$  is the amplitude of the electric field, and  $\Delta\Phi$  is the phase difference.

In an additive interferometer, the electric fields from the antennas are added together, resulting in a response  $E = E_1 + E_2 = 2E_0 \cos(\pi\nu\tau)$ . This response depends on the direction of the source ( $\theta$ ) and the baseline length ( $b$ ) relative to the observing wavelength ( $\lambda$ ).

In a multiplicative interferometer, the electric fields are multiplied, yielding a response  $E = E_1 \cdot E_2 = 2E_0 \cos(\pi\nu\tau)$ . This response also depends on  $\theta$ ,  $b$ , and  $\lambda$ , but lacks an offset term present in the additive interferometer.

The interferometer's response creates oscillatory patterns known as fringes, which depend on the source's position and the baseline length relative to the observing wavelength. These fringes allow astronomers to determine the properties of the observed source.

# Chapter 2

## Motivation and Objective

### 2.1 Motivation

SEAMS is a Radio telescope that is currently being designed to operate from 300 kHz to 16 MHz. Equipped with three sets of orthogonal electric and magnetic field sensors, this project is undergoing at SP Pune University and has been proposed to be developed in two phases.

In the first phase, the focus lies on utilizing electric field vector sensors to detect Radio Frequency Interference (RFI) in low earth orbit. The setup includes two orthogonal monopole antennas serving as electric field vector sensors, along with RF front-end components such as matching networks, filters, and gain stages for signal processing. Data acquisition and analysis are facilitated by a two-channel system with a Telemetry-Telecommand interface. The primary objectives of this phase include analyzing RFI emissions from Earth and detecting phenomena like Auroral Kilometric Radiation (AKR), atmospheric lightning, and solar bursts. Additionally, it aims to evaluate the feasibility of employing Commercial Off-The-Shelf (COTS) components for payload design in low earth orbit, thereby reducing production costs and simplifying upgrades for SEAMS Phase-2.

SEAMS Phase-2 will feature an expanded interferometric array of three orthogonal electric and magnetic sensors, with the payload positioned on the far side of the Moon or at the Moon-Earth L2 Lagrange point to mitigate Earth-originating RFI [27].

Inspired by Phase I & II of the Space Electric and Magnetic Sensor (SEAMS) mission, which is aimed to perform a Radio Frequency Interference (RFI) survey and test out interferometric principles respectively, we propose a mission wherein we will try to observe RFI scenario and perform an interferometer using a tethered system in this work. With this mission, we can get an insight into what other factors may affect the interferometer experiment of SEAMS phase II.

### 2.2 Mission Sequence

The proposed tethered CubeSat system will comprise a 2U and 1U CubeSat and will be launched as a combined 3U payload into Low Earth Orbit (LEO). Fig. 2.1

showcases the sequence of the tethered system. Upon reaching LEO, the 1U CubeSat will autonomously deploy from the 3U CubeSat. Once separated, the tethered CubeSat system will embark on its primary objective: astronomical observations utilizing radio interferometry techniques. This system will be equipped with an RFRI (Radio Frequency Interference (RFI) meter and Radio Interferometer) Instrument, to conduct meticulous surveys of the LEO environment to detect RFI sources.

The tethered setup of the CubeSats allows for the deployment of a two-element interferometer system, enabling precise measurements of radio sources in space. By showcasing the functionality of a two-element interferometer in LEO, this mission sets the stage for future advancements in space-based radio astronomy, providing valuable insights into the cosmos.

Through its dual mission of RFI detection and interferometric observation, this system promises to expand our knowledge of the universe while also addressing practical challenges in space-based radio astronomy.

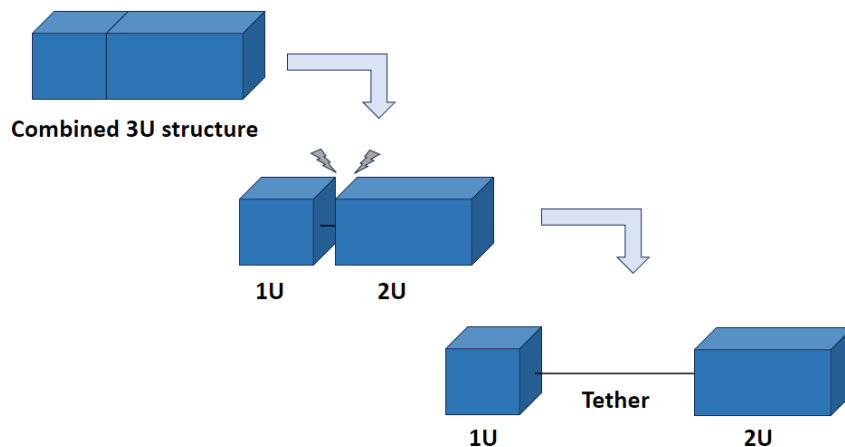


Figure 2.1: Mission sequence

## 2.3 Objectives:

The primary objective of this project is to demonstrate the feasibility and effectiveness of using a tethered CubeSat system for two-element radio interferometry in LEO. This study will involve:

- Design, development, and analysis of CubeSat structure.
- Design and development of RFRI (RFI meter and Radio Interferometer) instrument.
  - Design and development of patch antenna for RFI measurement and radio interferometry.
  - Development of digital backend for RFI measurement and interferometer.

# Chapter 3

## Proposed Payload

This project presents the development of a tethered CubeSat system designed to demonstrate two-element radio interferometry and Radio Frequency Interference (RFI) detection in Low Earth Orbit (LEO). The system leverages a modular design, utilizing two CubeSats: a 2U main satellite and a deployable 1U sub-satellite.

### 3.1 Subsystems:

#### 3.1.1 CubeSat Architecture:

- **2U Main Satellite:** This serves as the central hub, housing systems like the On-Board Computer (OBC), power management unit, communication unit, processing unit, etc.
- **1U Deployable Sub-Satellite:** This detachable module carries a secondary patch antenna and connects to the main spacecraft via a deployable tether.

#### 3.1.2 Deployment Mechanism of tethered system:

A reliable deployment mechanism will be employed to release the 1U sub-satellite from the 2U CubeSat at a predetermined distance (up to 5 meters) after reaching LEO. This mechanism ensures proper separation for effective interferometry. [33] presented a brief review of the existing mission deployment process of an on-orbit TSS (Tethered Satellite System). Three typical models for the space tether are discussed. The continuous model, discrete model, and rod model as per the paper is suitable for the study of the deployment dynamics and control methods, respectively. Most of the missions generally used two types of deployment mechanisms:

- A reel type deployer and
- A friction-type deployer

Mission-like Observations of Electric Field Distribution in the Ionospheric Plasma – a Unique Strategy(OEDIPUS): OEDIPUS-A and OEDIPUS-B, Tethered Satellite

System 1R (TSS-1R) [5]. Fig. 3.1 shows the deployer configuration of the OEDIPUS-A mission. The deployer includes a spool or reel that holds the tether in a compact and organized manner. During the mission, when the deployer receives the command to initiate tether deployment, the mechanism activates to unwind the tether from the spool. The reel-type deployer includes a mechanism for controlled deployment of the tether. This mechanism involves a motorized system, a spring-loaded mechanism, or other means of controlling the release of the tether from the spool. Missions like Small

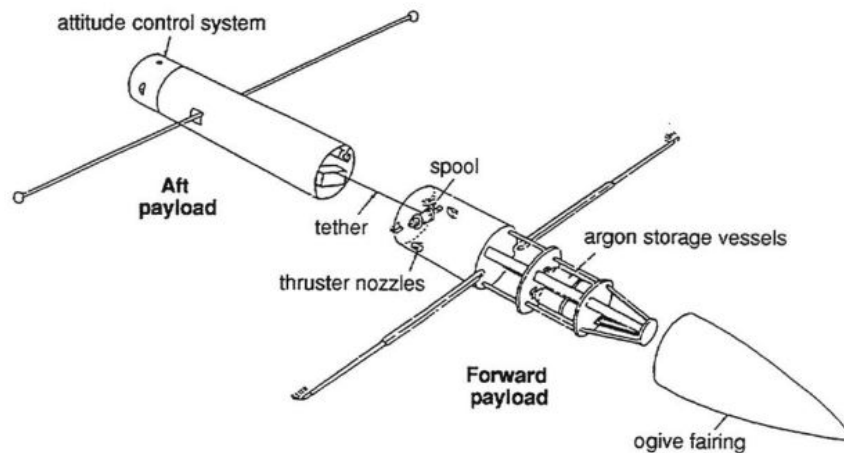


Figure 3.1: OEDIPUS-A payload configuration [5]

Expendable Deployer System (SEDS): SEDS-1 and SEDS-2 Missions, Plasma Motor Generator(PMG) adopted a friction type deployer. The deployer includes a friction-based mechanism that securely holds the payload in place during launch and while the satellite is in orbit. The payload, such as another satellite, instrument, or deployable structure, is securely attached to the friction-type deployer. This attachment point ensures that the payload remains in place until the deployer initiates the release sequence. When the satellite reaches the desired position or phase of the mission, a release command is sent to the friction-type deployer. This command triggers the mechanism to reduce friction or release its grip on the payload, allowing it to be deployed. Fig. 3.2 shows the functional diagram of the SEDS mission where the brake mechanism is connected to a motor driver for adjusting the friction grip to the tether. A sensor electronics is also attached to the deployer box, which will count the amount of turns that are deployed. Depending on the future tests planned, tether deployers will be selected.

### 3.1.3 Patch Antennas:

Both the 2U and 1U structures will be equipped with compact microstrip patch antennas. These antennas are designed and optimized for the desired operating frequency range suitable for RFI detection and for the demonstration of interferometric technology.

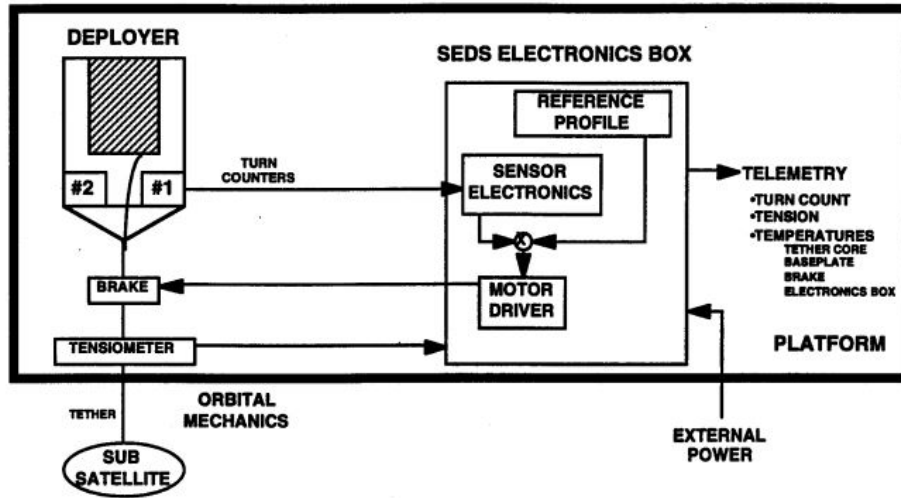


Figure 3.2: SEDS Functional Diagram [6]

Both the antennas will be connected via SMA cables along with the tether, reducing the need for synchronization between the antenna elements.

### 3.1.4 Backend Processing Unit:

The core of the interferometry system is a software-defined radio (SDR). This unit will be responsible for receiving, digitizing, and processing the radio frequency signals. The use of SDR allows for the implementation of various radio frequency (RF) signal processing algorithms and modulation schemes through software, enabling the system to adapt to different signal types and protocols without the need for hardware modifications. This flexibility makes SDR suitable for diverse applications and environments. Among the three available SDRs — RTL-SDR, LimeSDR Mini, and LimeSDR USB: LimeSDR USB is selected for its convenient ability to connect multiple antennas. By utilizing LimeSDR USB (LSU), the synchronization between the two antenna signals is simplified. LSU along with GNU radio is used for developing signal-receiving blocks and correlating the signals.

#### LimeSDR:

The LimeSDR-USB development board (Fig. 3.3) serves as a hardware foundation for creating and testing advanced digital and RF designs that require robust performance and intricate logic. It features Altera's Cyclone IV FPGA and Lime Microsystems transceiver, offering a versatile platform for prototyping various applications. Table 3.1 shows a brief of LimeSDR USB features and specifications.

- **Clock distribution:** The LimeSDR-USB board features a 30.72 MHz VCTCXO with initial precision of  $\pm 1$  ppm and stable precision of  $\pm 4$  ppm, serving as the reference clock for LMS\_PLLs. It can be tuned by an onboard phase detector or DAC, with automatic selection between them upon power-up. An external



Figure 3.3: LimeSDR-USB Development Board [7]

Feature	Description
RF Transceiver	Lime Microsystems LMS7002M MIMO FPRF
FPGA	Altera Cyclone IV EP4CE40F23 – also compatible with EP4CE30F23
USB 3.0 controller	Cypress USB 3.0 CYUSB3014-BZXC
Oscillator	Rakon RPT7050A @30.72MHz
Continuous frequency range	100 kHz – 3.8 GHz
Bandwidth	61.44MHz
RF connection	10 U.FL connectors (6 RX, 4 TX)
Power Output (CW)	Up to 10dBm
Multiplexing	2×2 MIMO
Power Supply	Via USB connector or optional external power supply
Status indicators	Programmable LEDs
Dimensions	100mm x 60mm

Table 3.1: LimeSDR-USB Development Board Features and specifications [7]

reference clock, ranging from 5 MHz to 400 MHz, can be supplied via the J19 U.FL connector for synchronization, allowing modification to bypass onboard circuitry. The Si5351C programmable clock generator can produce frequencies from 8 kHz to 160 MHz for FPGA and LMS PLLs.

- **Power distribution:** The LimeSDR-USB board offers flexibility in power options, accommodating both USB and external power sources. When USB power is inadequate, an external 6-12V power supply can be utilized. This external power can be connected via the J20 barrel power connector using a power plug (1.35mm ID, 3.5mm OD) or through pin header J21 (GND and VCC\_EXT). Notably, the board automatically selects the power source between USB and external, ensuring seamless operation. Additionally, polarity protection safeguards against incorrect connections, enhancing safety and reliability.

## **GNU Radio:**

GNU Radio is a free and open-source software toolkit that simplifies building software-defined radios (SDRs). Unlike traditional radios with fixed hardware circuits, SDRs perform signal processing in software on a computer. This allows for greater flexibility and customization. GNU Radio provides pre-built signal processing blocks that users can combine to create complex radio systems. These systems can be used for a wide range of applications, from basic audio processing to advanced communication protocols like GSM and satellite tracking. While not designed for specific radio standards out of the box, GNU Radio's modularity allows developers to build custom implementations for various communication needs. This eliminates the need for designing and debugging specialized hardware for each radio application.

The software offers a diverse array of pre-existing blocks covering various functions such as waveform generation, modulation, instrumentation (including GUIs), mathematical operations, channel modeling, filtering, and Fourier analysis. Users can seamlessly integrate these blocks into their signal processing flowgraphs to accomplish tasks like signal normalization, synchronization, measurement, and visualization. Moreover, GNU Radio allows users to develop custom blocks, either by combining existing ones intelligently to introduce new functionalities or by creating entirely new blocks that process input data and produce output data.

Setting up the GNU Radio application on Linux is straightforward, but for Windows users, Cygwin offers a solution. The GNU Radio Companion (GRC) Window, depicted in Fig. 3.4, provides a user-friendly interface. It involves selecting and dragging the required blocks onto the workspace to create the desired project flow. These blocks represent various signal-processing functions and components. By connecting these blocks in the desired sequence, users can design complex signal processing systems visually. Once the project is set up, users can configure the parameters and properties of each block through intuitive graphical interfaces. Finally, the project can be executed to process signals according to the defined flow.

### **3.1.5 On-Board Computer (OBC):**

The term "On Board Computer" simply means any unit that's on a satellite and can process information. However, when people refer to the On Board Computer or OBC, they usually mean the computer that is part of the satellite's avionics. This is where the On Board Software runs. The "On Board Software" isn't just any software; it's the one that's crucial for the satellite's key functions. Controlling the satellite's attitude and orbit, handling commands, collecting and organizing telemetry data, synchronizing time onboard, and responding to failures by detecting, isolating, and recovering from them are among these tasks.

The core component of an On Board Computer (OBC) is the microprocessor board. This board includes essential elements such as a microprocessor, non-volatile memories, volatile memories, and a companion chip facilitating connections between the microprocessor and various peripherals. This configuration forms the fundamental structure that enables the OBC to carry out crucial tasks, including running the On

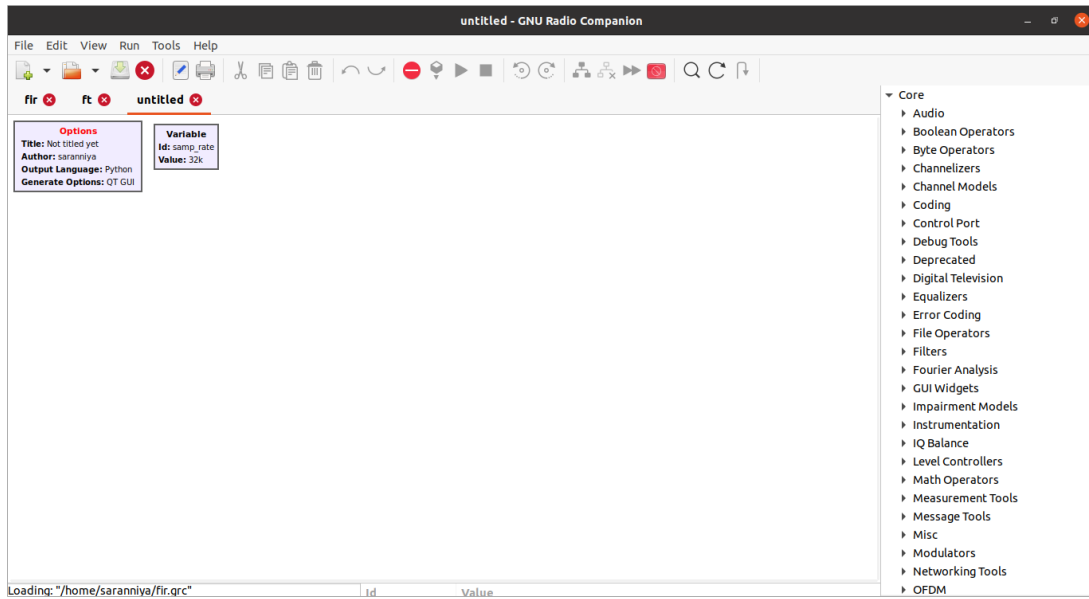


Figure 3.4: GRC Window

Board Software responsible for vital functions like controlling the satellite’s movements, executing commands, managing data, and responding to failures.

A modern On Board Computer not only has the processing capabilities mentioned earlier but also includes other functions within the same unit such as:

- Battery Management and Distribution
- Decoding Ground Station Commands
- Formatting packets for telemetry
- On Board time management
- Interfacing with other subsystems

When it comes to selecting an OBC for a CubeSat mission, there are several options available, each with its own set of advantages and considerations.

Three common choices for CubeSat OBCs are the Atmega 328p microcontroller, the STM32 F4/L+ series microcontroller, and the Raspberry Pi a single-board computer (SBC).

The Atmega 328p is a popular choice for CubeSat OBCs due to its simplicity, reliability, and low power consumption. It is a microcontroller commonly used in Arduino development boards. It is suitable for basic CubeSat missions with straightforward tasks such as data collection and telemetry. It is an excellent choice for cost-sensitive missions with power constraints.

The STM32 F4/L+ series microcontrollers offer more advanced processing capabilities compared to the Atmega 328p. These microcontrollers are based on the ARM Cortex-M architecture and provide higher clock speeds, more memory, and various peripherals. CubeSats equipped with STM32 OBCs can handle more complex tasks,

run sophisticated algorithms, and process data more efficiently. This option is ideal for CubeSats involved in missions that require advanced control and data processing capabilities.

Using a Raspberry Pi as the OBC board for a CubeSat brings the power of a full-fledged computer to space. Raspberry Pi is a credit-card-sized computer capable of running Linux-based operating systems. It offers considerable processing power, extensive memory, and support for a wide range of software applications. CubeSats with Raspberry Pi OBCs can execute complex tasks, run custom software, and perform tasks such as image processing or machine learning.

Feature	Atmega328P	STM32	Raspberry Pi
Architecture	8-bit AVR	32-bit ARM	ARM Cortex-A53 (32/64-bit)
Clock Speed	Up to 20 MHz	Varies (MHz to GHz)	1.2 GHz (Raspberry Pi 3 Model B)
Memory	Flash: 32 KB, RAM: 2 KB	Flash and RAM vary by model	Varies by model
GPIO Pins	23	Varies	40 (Raspberry Pi 3 Model B)
Communication	UART, SPI, I2C	UART, SPI, I2C, CAN, USB	GPIO, UART, SPI, I2C, USB, HDMI
Operating System	Bare-metal or simple OS	RTOS, Linux	Linux (Raspbian, etc.)
Power Consumption	Low	Varies	Moderate to High
Use Case	Simple embedded systems	Embedded systems, IoT	General-purpose computing

Table 3.2: Comparison of Atmega328P, STM32, and Raspberry Pi

In one part of this project, we will use Rasp pi as the onboard computer. As it has high processing power and memory capacity. This single board can be used for power handling, command handling, telemetry data processing, and RFI data processing.

### 3.1.6 Telemetry, Tracking and Command Handling

In order for space operations to continue operating as intended, satellites in orbit need to maintain communications with Earth, their mission controllers, and data users. TT&C, which stands for ‘Telemetry, Tracking, and Command’ involves receiving information about a satellite’s condition, figuring out where it is by tracking signals and sending instructions to the satellite. This applies to both manned spacecraft and unmanned satellites.

TT&C isn’t just about managing communication with a single spacecraft. It also involves handling connections between different spacecraft, like the communication link between an orbiter and a lander, or the connections between different satellites that enable them to share information and collaborate. Major tasks of TT&C include:

- Monitoring the satellite's well-being and condition by gathering, analyzing, and relaying data from its different subsystems.
- Pinpointing the precise whereabouts of the satellite by receiving, analyzing, and transmitting ranging signals.
- Effectively managing the satellite's operations by receiving, analyzing, and executing commands sent from the ground.

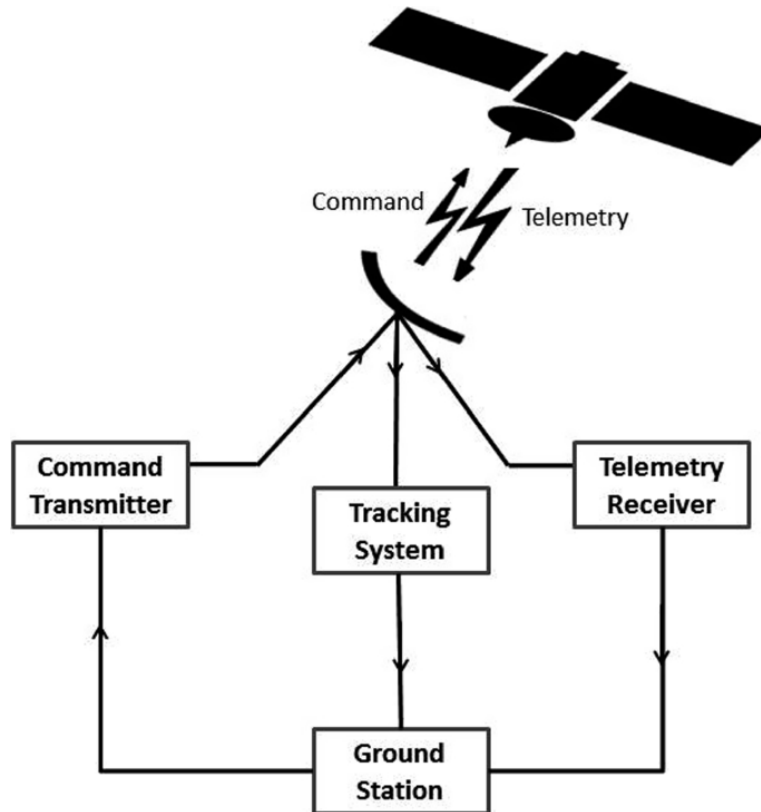


Figure 3.5: Telemetry, Tracking and Command System [8]

### Telemetry

This involves collecting and transmitting data from the spacecraft to the ground control station. The data could include information about the spacecraft's status, health, position, and various onboard parameters such as temperatures, power supply, voltages, and stored fuel pressure. Telemetry helps operators on Earth monitor the spacecraft and assess its performance.

### Tracking

Tracking involves determining the spacecraft's position and movement. Ground stations use tracking systems to follow the satellite as it orbits the Earth. Satellites emit

signals, known as beacon signals, which are received and processed by ground-based TT&C Earth Stations. This tracking is particularly important during the transfer and drifts orbital phases that follow the satellite's launch, ensuring it reaches the intended orbit and maintains the correct position. To periodically determine the satellite's range from the ground station, the system measures the propagation delay of signals, aiding in accurate positioning and effective management of the satellite's operations. This information is crucial for maintaining communication and understanding the spacecraft's trajectory.

### **Command Handling**

Command handling refers to the process of sending instructions or commands from the ground control station to the spacecraft. These commands can be related to adjusting the spacecraft's orientation, activating specific instruments, or performing other maneuvers. This two-way communication allows operators to control and manage the satellite's operations. To prevent unauthorized access and decoding, command signals are often encrypted.

### **3.1.7 Electric Power System**

Like any other equipment, a satellite needs electricity to run. Although it launches from Earth using an onboard battery at first, this limited supply from its home planet is not enough for sustained, long-term functioning over a period of time. Consequently, longer-lasting power sources are required for continuous operation.

Power Systems in space cover everything related to generating, storing, and managing power for different types of space missions. These missions can range from a few minutes, like launchers, to decades. The key challenge in Power Systems engineering is to find the best combination of primary and secondary power sources, along with the right system architecture, to ensure optimal performance. Launchers typically use electrochemical sources like primary or secondary batteries. Satellites in Earth's orbit often rely on solar generators and batteries, especially when they are not exposed to the Sun, such as during launch or when in the Earth's shadow. Modern satellites commonly use advanced solar cells with around 30% efficiency and Lithium-ion batteries.

For a space mission to work well, it needs a constant and dependable power source and the Sun is a great supplier, providing about 1.4 kilowatts of power per square meter in Earth's orbit. Spacecraft designers try their best to make use of this abundant resource, that's why most spacecraft have wing-like solar arrays or layers of solar panels on their surface. These solar arrays are made up of photovoltaic cells linked together. When sunlight hits these cells, they generate an electrical current. This generated electrical power is then harnessed to run the satellite's various subsystems, ensuring its functionality and success in the mission.

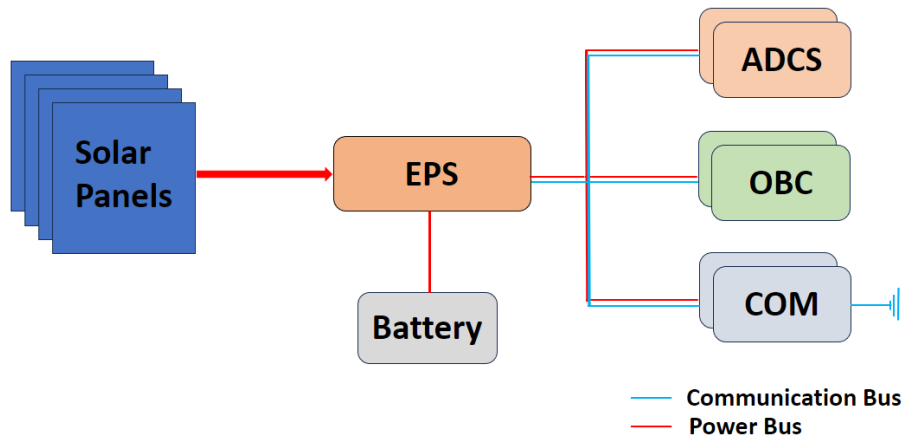


Figure 3.6: Basic EPS Block

### 3.1.8 Attitude Determination and Control System

Attitude Determination and Control System (ADCS) is a crucial component of a spacecraft responsible for controlling its orientation (attitude) in space. The ADCS system helps a spacecraft achieve and maintain a desired orientation, ensuring that it is pointed in the right direction for its mission objectives when external disturbances like solar radiation pressure, gravitational forces, or atmospheric drag come into play. To accurately determine the spacecraft's current orientation, sophisticated sensors like gyroscopes, accelerometers, and star trackers are employed. These instruments provide precise measurements that serve as the foundation for the ADCS system's operations.

The Attitude Determination and Control System (ADCS) consists of four modules, and each module has its own goals:

- Sensors module comprising a set of sensors that gather data to understand where the CubeSat is positioned.
- The Actuators module involves CubeSat attitude actuators. Their job is to adjust the CubeSat's orientation based on the mission requirements.
- The Controller module of the ADCS has the task of collecting data from sensors, processing it to obtain reliable positioning information, and then sending commands to the actuators module to correct or modify the CubeSat's attitude. This is done if permitted by the On-Board Computer (OBC) and Electrical Power System (EPS) subsystems.
- The Interface module aims to maintain a good connection with other satellite systems and transmit data to these systems. It ensures effective communication between the ADCS and the other components of the satellite.

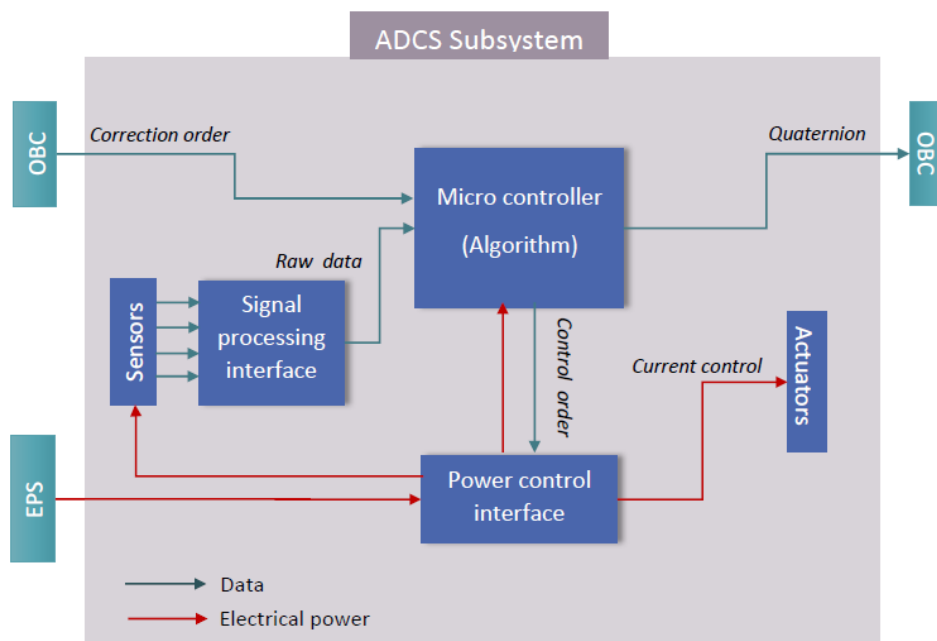


Figure 3.7: Block diagram of ADCS System [9]

### ADCS Sensors

- **Gyroscope** : It is an instrument that uses the concepts of angular momentum to measure or maintain orientation. Gyroscopic stability is the fundamental concept behind a gyroscope. According to this principle, a spinning object tends to maintain its axis of rotation unless an external force is applied. This property makes gyroscopes valuable in various applications, particularly in navigation systems, aircraft, spacecraft, and other devices where precise orientation is crucial.
- **Sun sensor** : A sun sensor is a device designed to detect and determine the direction of sunlight. It plays a crucial role in spacecraft and satellite systems for attitude determination and control. The basic function of a sun sensor is to provide information about the position of the sun relative to the spacecraft, allowing for precise orientation and alignment.

Sun sensors typically consist of photodiodes or other light-sensitive elements arranged in a specific pattern. When sunlight strikes these sensors, the amount and distribution of light on the sensors provide valuable data about the sun's position. By analyzing this information, the spacecraft's onboard systems can adjust its orientation to align with the sun or maintain a desired attitude.

- **Magnetometer** : It is a device used to measure the strength and direction of a magnetic field. The fundamental principle behind a magnetometer is the interaction between magnetic fields and the sensor's components, which allows for the detection and measurement of magnetic phenomena.

Magnetometers can be based on different technologies, such as fluxgate, proton

precession, or Hall effect sensors. These sensors can detect changes in the magnetic field caused by nearby magnetic materials, electric currents, or the Earth's magnetic field.

### **Actuators**

- **Reaction wheel :** Reaction wheels (RW) serve as the main method for spacecraft attitude control. These wheels consist of a flywheel connected to an electric motor, causing it to rotate as the motor operates. According to Newton's third law, the CubeSat will then initiate a counter-rotation. Since a single reaction wheel can only induce rotation around one axis, three of them would be required.
- **Magnetorquer :** A magnetorquer, also known as a magnetic torquer, functions as a system for attitude control, detumbling, and stabilization by leveraging the interaction between a generated magnetic dipole and the Earth's magnetic field. This interaction produces a torque that is utilized to manage the satellite's rotation around its center of gravity.

# Chapter 4

## Design and Development

### 4.1 CubeSat Chassis

The importance of a CubeSat chassis lies in its role as the structural foundation for the entire satellite. Serving as the outer framework, the chassis provides structural integrity, support for various components, and a means to integrate and protect the satellite's payload and subsystems. The design of the chassis directly influences the satellite's overall stability, durability, and performance in space. Moreover, the CubeSat chassis is crucial for meeting standard CubeSat form factors, ensuring compatibility with launch vehicles, and facilitating cost-effective and standardized satellite development. Due to the significance of CubeSats in space applications and subsystem development, different structures have been designed, analyzed, and modified to meet evolving mission requirements. The structure is designed and analyzed utilizing the finite element method. This process helps identify its natural frequencies and mode shapes, assess its stress levels during launch, and ensure durability against challenging space environment factors like solar radiation, Earth's albedo, and infrared emissions (Fig. 4.1).

The amount of sunlight exposure varies based on factors such as orbit altitude, inclination, and epoch [34]. In particular, the period  $T$  of a circular orbit at an altitude  $h$  is given by

$$T = 2\pi\sqrt{\frac{(R + h)^3}{\mu}} \quad (4.1)$$

with  $R$  Earth's radius and  $\mu$  Earth's standard gravitational parameter. Therefore, for an orbital altitude of 600 km, taking  $R = 6371$  km and  $\mu = 3.986 \times 10^5 \text{ km}^3/\text{s}^2$ , the period of the CubeSat is determined as 5792 s.

In order to estimate the time in sunlight (TS) and maximum time of eclipse (TE),

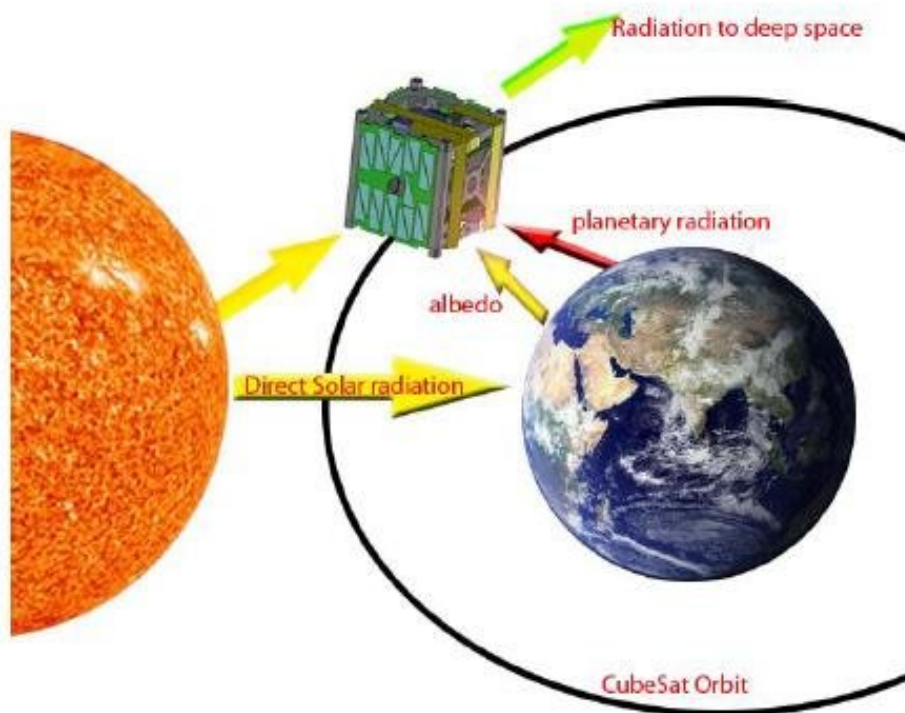


Figure 4.1: Heat Flux Sources for a CubeSat [10]

we first need to estimate the angular radius at mission altitude [10]:

$$\begin{aligned}
 \rho &= \sin^{-1} \left( \frac{R}{R+h} \right) \\
 &= \sin^{-1} \left( \frac{6371}{6371+600} \right) \\
 &= 66^\circ
 \end{aligned}$$

$$\begin{aligned}
 TE &= \frac{2\rho}{360^\circ} \times T \\
 &= \frac{2 \times 66}{360} \times 5792 \\
 &= 2123 \text{ sec}
 \end{aligned}$$

$$\begin{aligned}
 TS &= T - T_E \\
 &= 5792 - 2123 \\
 &= 3669 \text{ sec}
 \end{aligned}$$

Heat fluxes related to solar radiation, the Earth's albedo, and infrared energy are calculated as  $1363 \text{ W/m}^2$ ,  $406 \text{ W/m}^2$ , and  $237 \text{ W/m}^2$ , respectively. In the worst-case scenario, one side of the CubeSat receives direct solar radiation, while an adjacent side facing the Earth experiences the combined heat flux of albedo and Earth's infrared

energy. To ensure the CubeSat design's thermal safety, one side is subjected to a heat flux of  $1363 \text{ W/m}^2$ , while an adjacent side receives a combined flux of  $406 \text{ W/m}^2$  (albedo) and  $237 \text{ W/m}^2$  (Earth's infrared energy) [10] [35].

#### 4.1.1 Design & Modelling of 1U structure

The design and modeling process utilized CATIA v5 software. Initially, we started with a standard cube design for a 1U CubeSat chassis, which was later transformed into two configurations, one with reduced structural mass illustrated in Fig. 4.2. To enable a miniature space mission, a preliminary design was created, measuring  $100 \text{ mm} \times 100 \text{ mm} \times 100 \text{ mm}$ , adhering to the 1U CubeSat category designed for Pico-satellites weighing between 0.1 and 1kg [36].

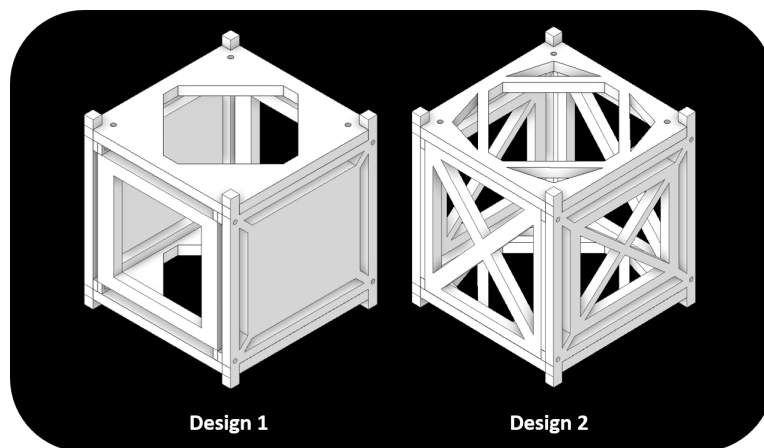


Figure 4.2: CAD Model

The Structural and Thermal Analysis was conducted using the ANSYS 2023 R2 software (student version). The Structural Analysis seeks to evaluate structural integrity by subjecting different points across the configuration to varying loads. Using default settings, a mesh size of 52,708 elements and 92,982 nodes were constructed in the model. Both models depicted in Fig. 4.3 underwent testing, exposed to 15g and 6g loads in three distinct scenarios, with forces applied to the top surface, walls, and side edges, keeping the bottom side fixed.

Thermal analysis was done at temperatures ranging from  $-100^{\circ}\text{C}$  to  $300^{\circ}\text{C}$ , along with a convection coefficient of  $10 \text{ W/m}^2\text{C}$  applied at  $22^{\circ}\text{C}$ . The mesh nodes and elements kept consistent with the structural analysis, ensuring that the computational model maintained accuracy and alignment with the physical characteristics of the CubeSat designs.

#### 4.1.2 Result

Following a comprehensive structural and thermal analysis of both the conventional CubeSat and the optimized modular CubeSat design, the outcomes were meticulously evaluated. In terms of structural performance, when subjected to diverse load orientations, the optimized design exhibited superior behavior, particularly under 6g loads.

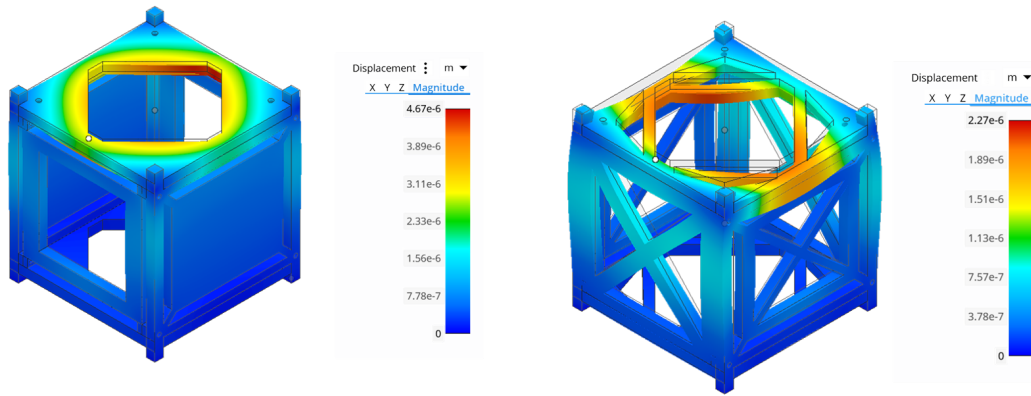


Figure 4.3: Structural Simulation

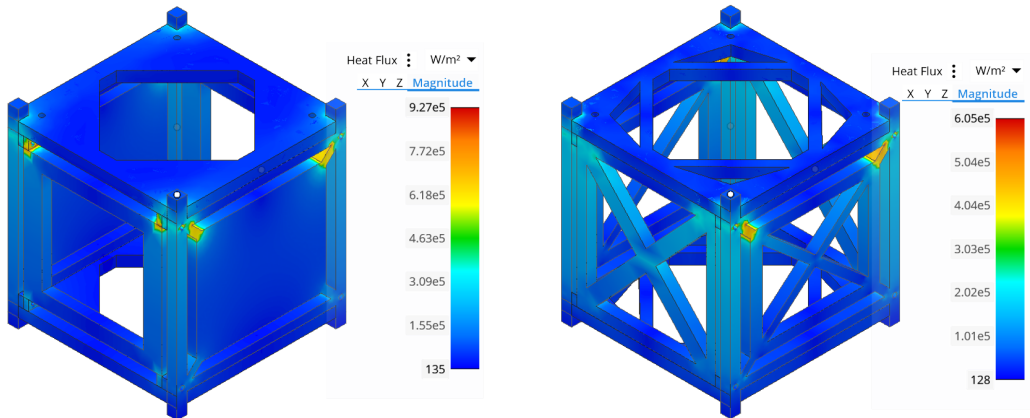


Figure 4.4: Thermal Simulation

Notably, it displayed reduced deformation compared to the conventional CubeSat. Specifically, when subjected to top-loading forces, the optimized CubeSat demonstrated a deformation of merely  $0.908 \mu\text{m}$ , in contrast to the conventional CubeSat's  $1.86 \mu\text{m}$  deformation. Furthermore, when subjected to loads along the walls and edges, the optimized structure displayed slight but consistent improvements in structural resilience. In thermal analysis, the optimized modular CubeSat design excelled by exhibiting notably lower heat flux values. Lower heat flux implies that the CubeSat's body is less susceptible to the transmission of heat from the surrounding environment. This thermal advantage enhances the CubeSat's ability to regulate its internal temperature effectively. Collectively, the optimized CubeSat design outperformed the conventional CubeSat in both structural and thermal aspects, underscoring its suitability for space missions demanding robust structural integrity and superior thermal control. It is observed that Design 1 undergoes less deformation when subjected to load and also has less force and temperature distribution along the body, whereas Design 2 has better force and temperature distribution ( Fig. 4.3 and 4.4). Table 4.1 and table 4.2 show the summary of structural and thermal analysis respectively. This shows that the modular hollow design provides better load and temperature distribution while simultaneously

PARAMETERS	DESIGN-1	DESIGN-2
<b>MASS</b>	0.705kg	0.578kg
<b>G-FORCE</b> (Deformations along the direction of force)		
On Top surface (15G)	4.67 $\mu m$	2.27 $\mu m$
On Top surface (6G)	1.86 $\mu m$	0.908 $\mu m$
On walls (15G)	24.1 $\mu m$	11.7 $\mu m$
On walls (6G)	9.63 $\mu m$	4.69 $\mu m$
On edges (15G)	17 $\mu m$	11 $\mu m$
On edges (6G)	6.8 $\mu m$	4.7 $\mu m$

Table 4.1: Summary for Structural Analysis.

TEMPERATURE ( $^{\circ}C$ )	HEAT FLUX ( $\phi$ ) ( $W/m^2$ )	HEAT FLUX ( $\phi$ ) ( $W/m^2$ )
	DESIGN - 1	DESIGN - 2
-100	$4.07 \times 10^5$	$2.66 \times 10^5$
0	$7.33 \times 10^4$	$4.79 \times 10^4$
100	$2.6 \times 10^5$	$1.7 \times 10^5$
200	$5.93 \times 10^5$	$3.88 \times 10^5$
300	$9.27 \times 10^5$	$6.05 \times 10^5$

Table 4.2: Summary for Ambient Thermal Analysis

reducing the mass of the payload. This is beneficial as it allows for more efficient payloads and helps to reduce the cost of satellite launches.

### 4.1.3 Design & Modelling of 2U structure

Further, A modular 2U design, with dimensions of 10cm x 10cm x 20cm, is created using CAD tools (Fig. 4.5 ) and utilized Finite Element Analysis (FEA) to optimize the design of a 2U CubeSat for an RFI detection and localization mission. By analyzing two different modular configurations, FEA helps us achieve a balance between structural integrity and thermal management, ultimately leading to a more reliable and efficient CubeSat design.

### 4.1.4 Result

#### Structural and Thermal Analysis

Using default settings, a mesh size of 16,594 elements and 32,026 nodes were constructed. Both models depicted in Fig 4.6 underwent testing, exposed to 16g with force applied to the top surface keeping the bottom side fixed. The analysis was conducted incorporating a temperature ranging from  $-65^{\circ}C$  to  $150^{\circ}C$ , along with a convection coefficient of  $5 \times 10^{-6} W/mm^2 \text{ } ^{\circ}C$  applied at  $22^{\circ}C$ .

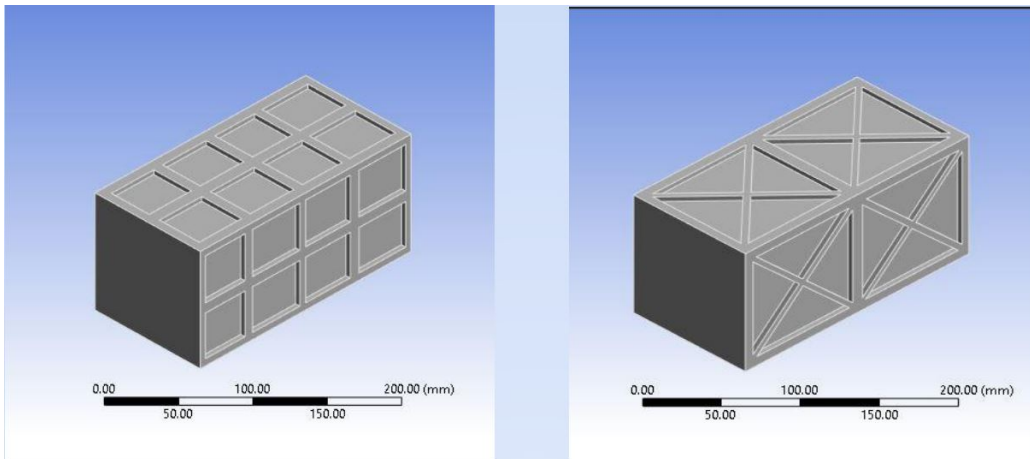


Figure 4.5: Modular 2U designs

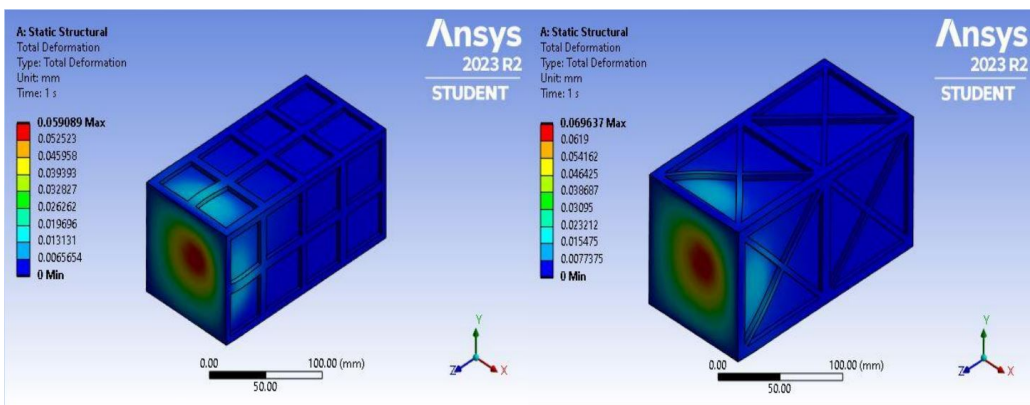


Figure 4.6: Total deformation of the two modular structures under 16g

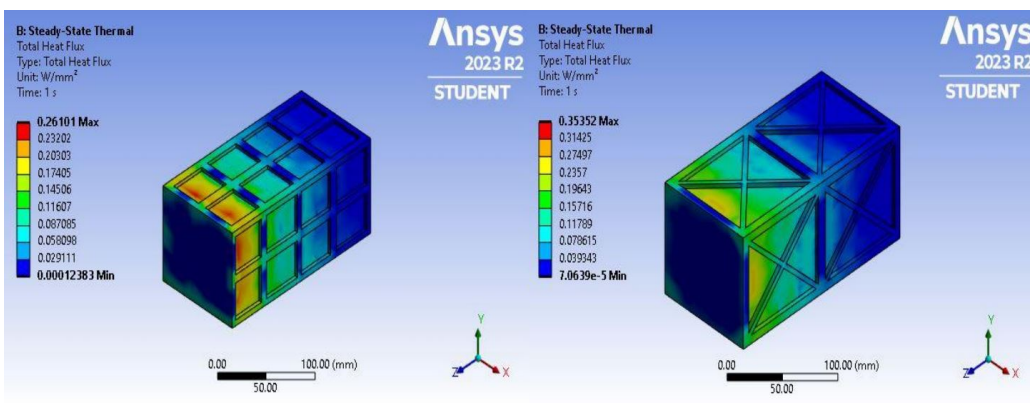


Figure 4.7: Total heat flux of the two modular structures

### Modal Analysis

Structures can vibrate excessively when subjected to external forces at their natural frequencies. This resonance can lead to catastrophic failures. Modal analysis helps

identify these natural frequencies so engineers can design structures to avoid resonance during operation. This analysis examines the natural frequencies of a CubeSat structure within a range of 0 to 6000 Hz. This evaluation adheres to the guidelines set forth by the user's guide for the Polar Satellite Launch Vehicle (PSLV). As per regulations governing the PSLV launch vehicle, payloads must possess adequate structural stiffness. This requirement ensures that the fundamental frequencies of CubeSats, especially at the attachment point to the launch vehicle, surpass specified thresholds. These thresholds are set at 35 Hz along the rocket's length (longitudinal axis) and 20 Hz perpendicular to its long axis (lateral axis). Additionally, during launch, there will be significant harmonic frequencies below 100 Hz. Hence, the natural frequencies of the CubeSat need to exceed 100 Hz to avoid resonance. [35]. To prevent resonance, a phenomenon that can cause catastrophic failures, the calculated natural frequencies from our analysis need to be higher than these minimum constraint values. In simpler terms, the CubeSat needs to be stiff enough to vibrate at frequencies above the limits set by the PSLV to avoid harmful resonance during launch. The analysis revealed that the first vibration mode frequency is slightly higher for the square-framed structure (1126.8 Hz) compared to the triangular-framed one (1122.8 Hz) as shown in Fig. 4.8.

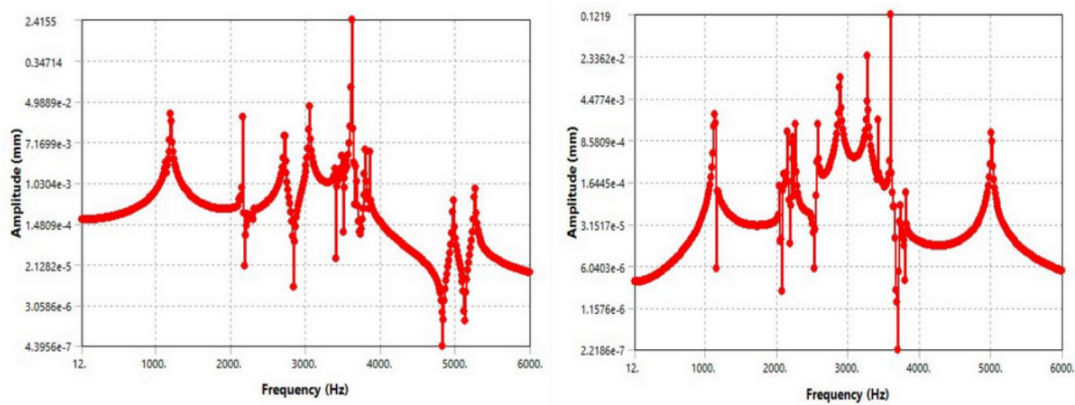


Figure 4.8: Harmonic response graph of both cubesat structure

Design	Mass(Kg) ( $^{\circ}C$ )	Total Deformation (16G)(mm)	HEAT FLUX ( $\phi$ ) ( $W/m^2$ )
Design 1	1.0933	0.059089	0.26101
Design 2	0.96761	0.069637	0.35352

Table 4.3: Comparison Table of both structures

The analysis of both modular designs for the 2U CubeSat yielded positive results. The structures experienced minimal overall deformation relative to their size. Additionally, the Von Mises stress values, around 18 MPa and 16 MPa, fall well within acceptable limits considering the high yield strength (276 MPa) of the chosen aluminum alloy (AL-6061).

Given its lower mass, the triangular frame was chosen as the baseline design. We then incorporated additional features and modifications to the structure to align with the project's specific requirements.

### 4.1.5 3U Modular Structure

Both the modified 1U and 2U structures are combined into a 3U CubeSat system (Fig. 4.9). Structural, thermal, and modal analyses were meticulously conducted on the chassis to assess its initial integrity. Analysis was conducted using the ANSYS 2023 R2 software (student version). Using default settings, a mesh size of 32,534 nodes and 15,158 elements was constructed in the model using Al6061-T6 as chassis material.

#### Modal Analysis:

Modal analyses are conducted using an empty CubeSat structure to ensure a conservative analysis, avoiding any additional stiffness introduced by onboard components. The results of this analysis, excluding free body motion modes, are presented in Table 4.4.

Mode	Frequency(Hz)
1	1856.2
2	2035.8
3	2055.2
4	2446
5	2448.3
6	2450.5
7	2494.8
8	3104.2
9	3178
10	3351.3

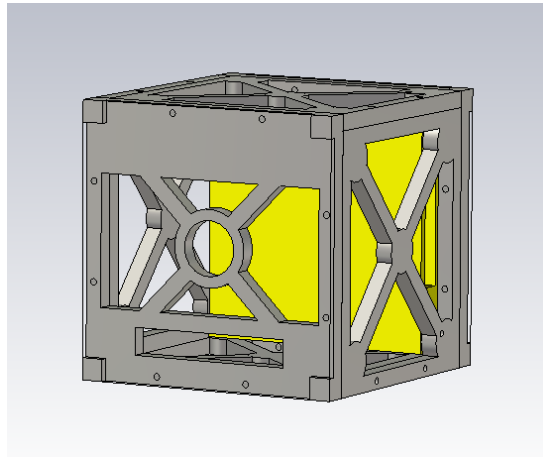
Table 4.4: Modal Analysis of 3U combined structure

As mentioned earlier, the CubeSat's natural frequencies must exceed 100 Hz to prevent resonance. According to the findings, the lowest mode is approximately 1856.2 Hz (Table 4.4), significantly surpassing the critical threshold of 100 Hz, thus meeting the acceptability criteria

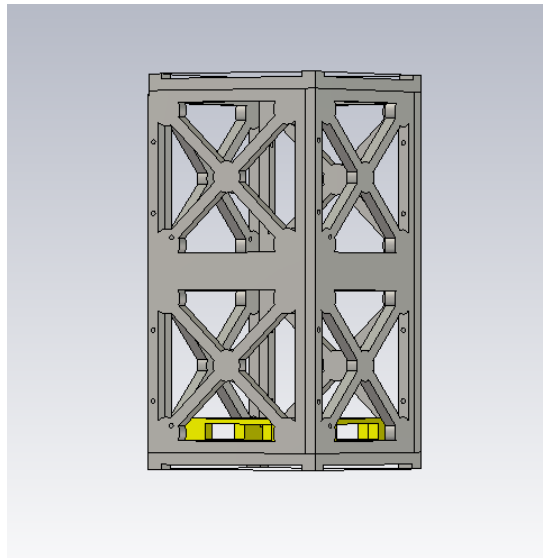
#### Structural Analysis

During the launch phase, the CubeSat must withstand the acceleration loads associated with the launch process. To assess the stress levels induced by these acceleration loads, quasi-static launch analyses are conducted. For the Polar Satellite Launch Vehicle, the quasi-static launch loads amount to 11 g along the "z" axis and 6 g each along the "x" and "y" axes [35]. The model, depicted in Fig. 4.11, was subjected to testing with the bottom side held fixed.

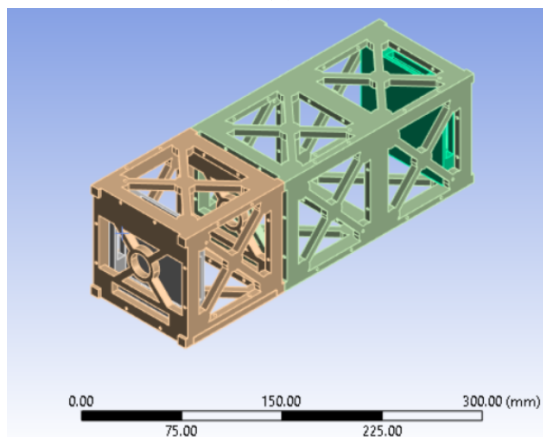
Further, the analysis was overloaded, by applying 16g [37] in all x, y, and z directions to give more confidence in the structural design and also to encompass more launch vehicles. Table 3.5 summarizes the structural response of the analyzed system under different loading scenarios.



(a)

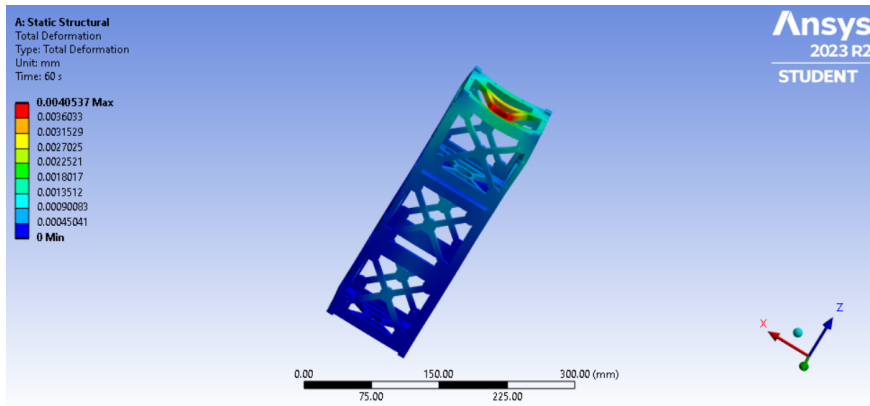


(b)

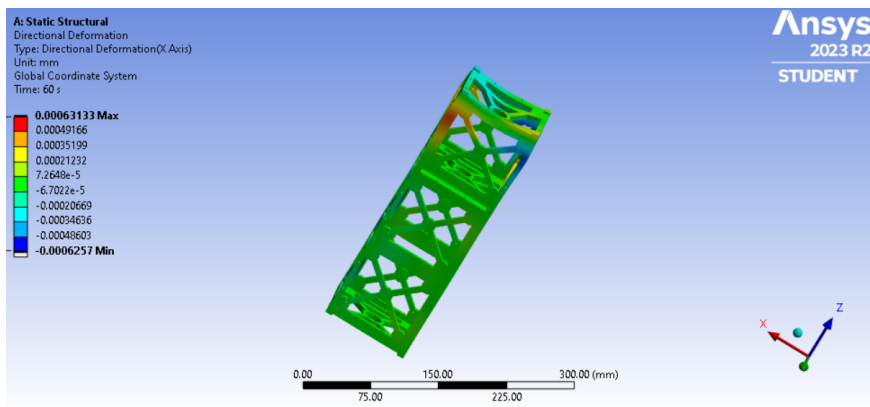


(c)

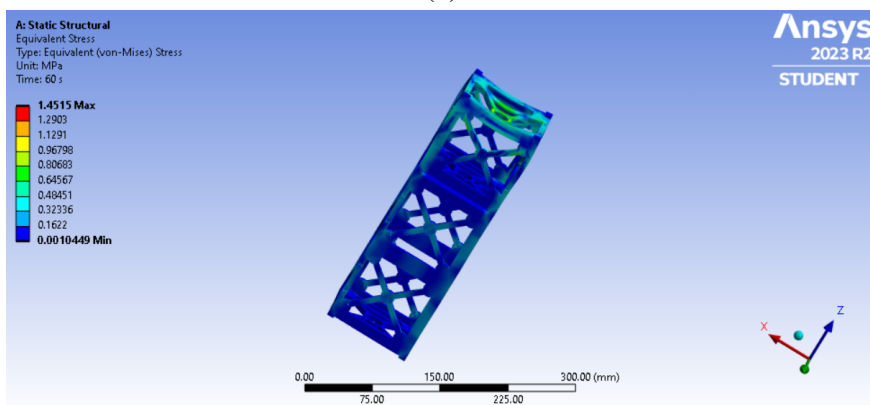
Figure 4.9: (a) Modified 1U structure (b) Modified 2U structure (c) Combined 3U structure



(a)

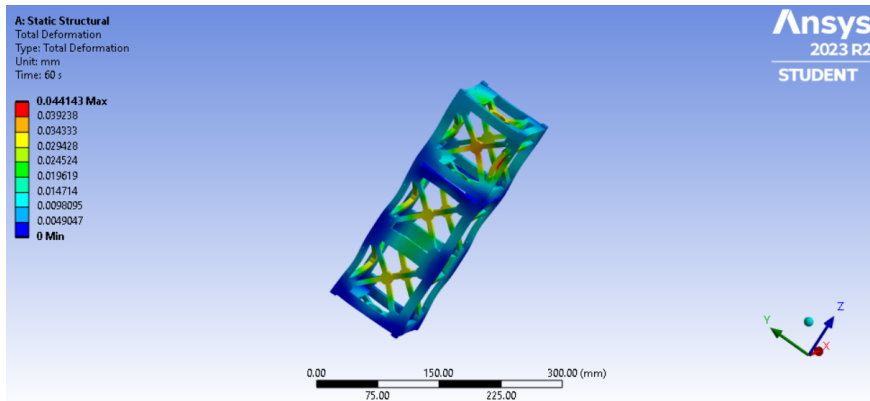


(b)

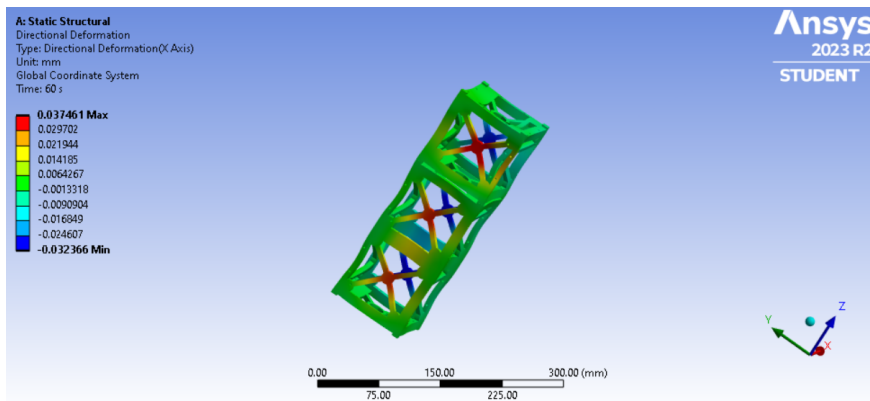


(c)

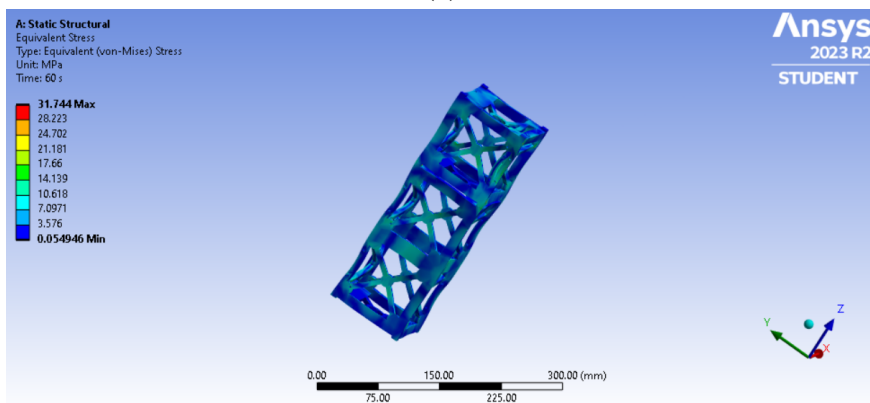
Figure 4.10: (a) Total Deformation (b) Directional Deformation (c) Equivalent (von Mises) stress distribution, subject to static loads of 11 g in the “z” axis and 6 g in both for “x” and “y”



(a)



(b)



(c)

Figure 4.11: (a) Total Deformation (b) Directional Deformation (c) Equivalent (von Mises) stress distribution, subject to static loads of 16g in x,y and z direction simultaneously

The structural analysis reveals that the structure remains within safe limits, as evidenced by maximum stresses of 1.4515 MPa and 31.744 MPa, respectively. These values are well below the yield strength of aluminum 6061-T6, set at 276 MPa, suggesting the structure can withstand yielding under the applied loads. Additionally, the maximum total deflection recorded at 0.0040537 mm and 0.044143 mm indicates minimal deformation, further affirming the structural integrity during launch conditions.

Load in each direction	Total Deformation(mm) (max)	Directional Deformation (mm) (max)	Equivalent (von-mises) Stress (MPa) (max)
x=y=6g, z=11g	0.0040537	0.00063133	1.4515
x=y=z=16g	0.044143	0.037461	31.744

Table 4.5: Deformation and stress results for a structural analysis under different loading conditions

It's important to note that this analysis focuses solely on the chassis. The overall response may vary once all components are integrated, warranting a comprehensive reanalysis.

### Thermal Analysis

The analysis was conducted incorporating a temperature ranging from -65°C to 150°C, along with a convection coefficient of  $5 \times 10^{-6} \text{ W/mm}^2 \text{ }^\circ\text{C}$  applied at 22°C.

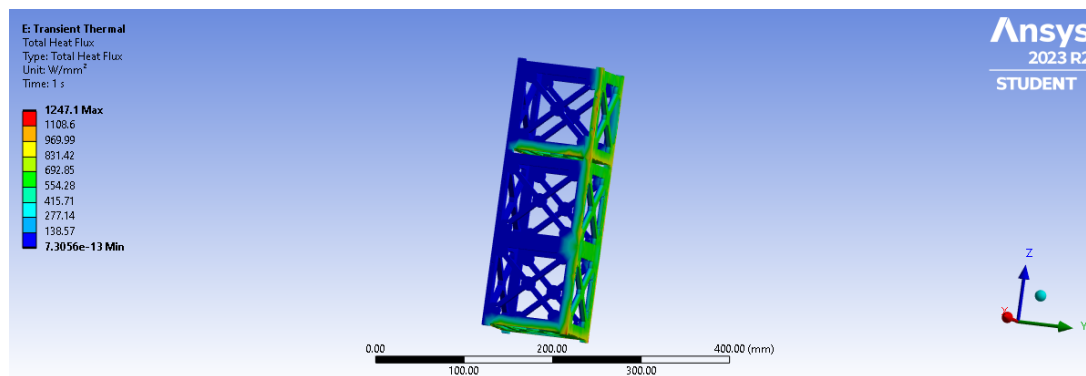


Figure 4.12: Thermal Simulation

Minimum [W/mm <sup>2</sup> ]	Maximum [W/mm <sup>2</sup> ]	Average [W/mm <sup>2</sup> ]
7.3056e-013	1247.1	181

Table 4.6: Flux Distribution in the CubeSat

Table 4.6 presents the flux distribution in a CubeSat, indicating the minimum, maximum, and average values of heat flux measured in watts per square millimeter.

These metrics are crucial in understanding the thermal behavior of the CubeSat, particularly in extreme conditions.

In an extreme scenario, where one side of the CubeSat is exposed to direct solar radiation while an adjacent side faces both the albedo and Earth's infrared energy, the design must ensure thermal safety. High heat flux can impact the structural integrity of CubeSats. Differential heating across the spacecraft can lead to thermal stresses, potentially causing deformations or structural failures. By understanding heat flux, engineers can design structures that can withstand thermal loads experienced in space. In this context, the flux from surrounding sources appears to have a lesser impact on the CubeSat.

## 4.2 Antenna Design

### 4.2.1 Design

To fulfill the mission requirements of radio interferometry while adhering to the size constraints of a CubeSat form factor, a simple microstrip patch antenna was designed and optimized using CST Studio software. The antenna utilizes an FR-4 substrate with dimensions of  $100\text{ mm} \times 100\text{ mm}$ .

This study presents the design of an inset feed microstrip patch antenna [38] with a patch size measuring  $64 \times 49\text{ mm}$ . The antenna employs a substrate made of FR-4 material with a dimension of  $100\text{ mm} \times 100\text{ mm}$ , possessing a thickness of  $1.6\text{ mm}$ . The substrate has a dielectric constant of  $4.3$ , loss tangent equal to  $0.02$ . This rectangular patch is excited using a transmission line of a width of  $3\text{ mm}$ .

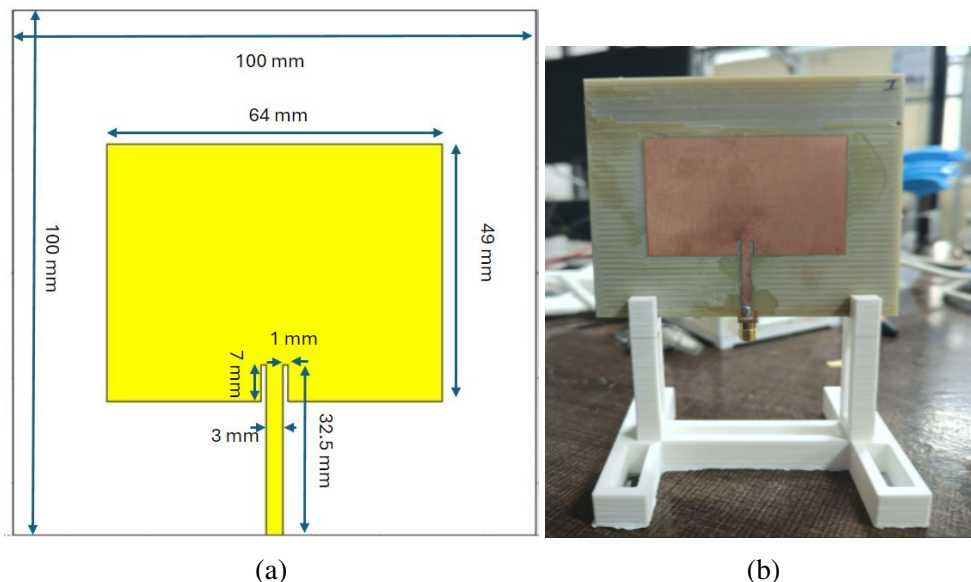
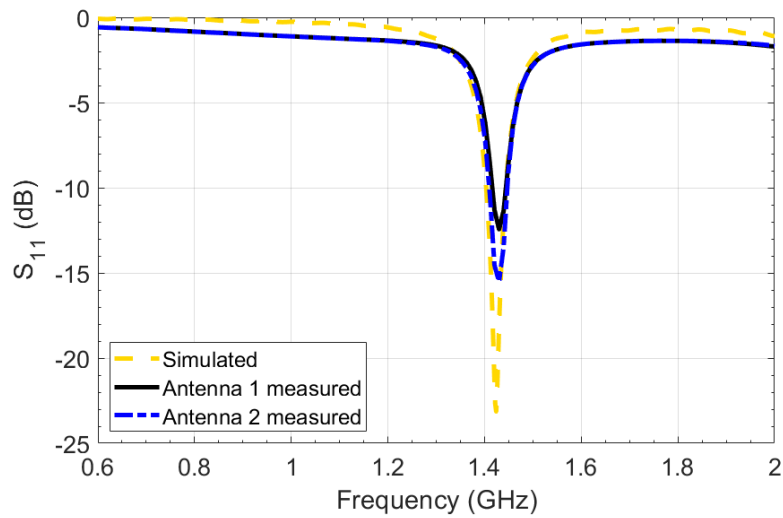


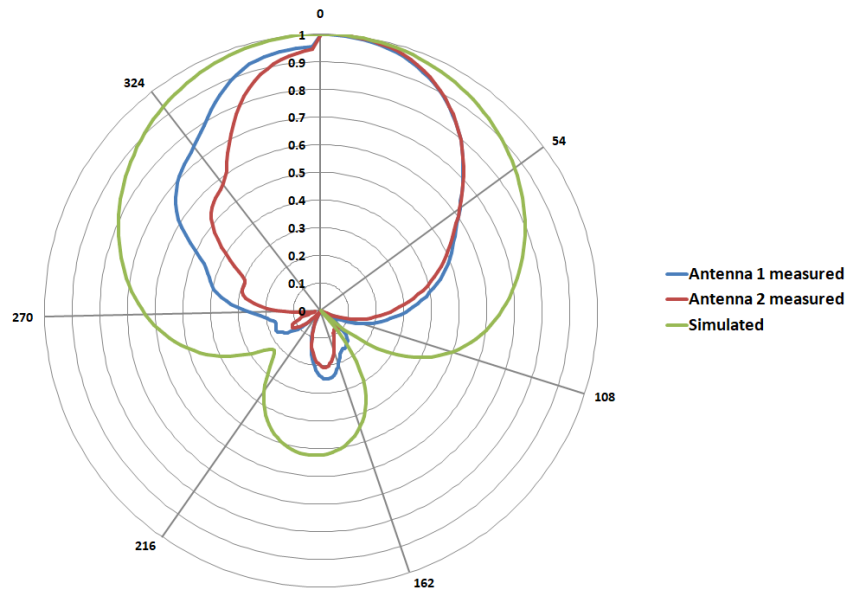
Figure 4.13: (a) Schematic of the inset feed microstrip patch antenna (b) Fabricated inset feed microstrip patch antenna

## 4.2.2 Result

The  $S_{11}$  (Return Loss) parameter indicates the amount of power that is lost to the load and does not return as a reflection. Fig.4.14a illustrates the simulated result of The S parameter  $S_{11}$  depicts a return loss of about -22.82 dB at the 1.424 GHz band frequency with a bandwidth of 38.7 MHz in CST. The antenna radiation pattern is the functional demonstration of the antenna radiation fields through which the behavior of the antenna radiation power can be specified over long distances in various spatial directions (Fig.4.14b). Table 4.7 shows the simulated and measured parameters of the patch antenna.



(a)



(b)

Figure 4.14: (a)  $S_{11}$  (b) 2D radiation pattern of simulated and measured patch antenna

Parameters	Simulation	Antenna 1	Antenna 2
$S_{11}$ (dB)	-23.032	-15.8	-13.2
Half Power Beam Width(HPBW)	93.8°	55.8°	50.4°
Gain(dB)	1.43	2.424	2.617

Table 4.7: Simulated and measured parameter of patch antenna

# Chapter 5

## The RFRI Instrument

### 5.1 RFI meter

#### 5.1.1 Block Diagram:

Fig. 5.1 depicts a fundamental block diagram illustrating the components of an RFI collection system. At the forefront, an antenna is connected to a low noise amplifier (LNA), followed by a Band Pass Filter (BPF). Subsequently, the signal undergoes processing through a Software-Defined Radio (SDR). The SDR converts the signals to a baseband before sampling and converting them to a digital signal for storage. The data is stored in the SBC's storage unit for post-processing.

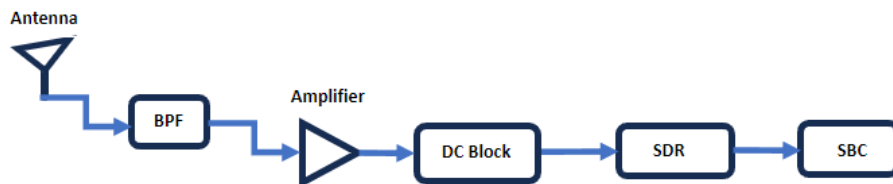


Figure 5.1: RFIM block diagram

The front end utilizes a patch antenna tuned to resonate at a frequency of 1.42 GHz. A Nooelec LNA, accompanied by the LimeSDR USB is connected to Raspberry Pi (Raspi) as the Single Board Computer (SBC) (Fig. 5.2).

GNU-Radio scripts are used in the digital backend to accomplish desired recording qualities and data formats. The instrument has one channel which receives a signal directly from the antenna. The signals are then filtered, amplified, and connected to the LimeSDR USB. This radio converts the signals to a baseband before sampling and converts them to a digital signal for storage.

In the GNU Radio block diagram, a LimeSDR source block serves as the intermediary between the SDR hardware and the GNU Radio software. The incoming signal is

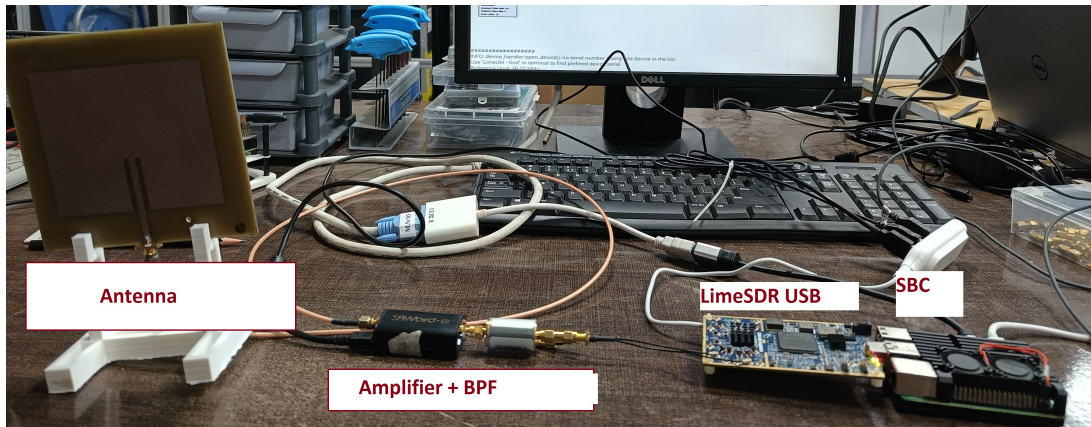


Figure 5.2: RFIM Lab Setup

subjected to Fast Fourier Transform (FFT), followed by data averaging. Subsequently, the processed data is stored for later post-processing tasks. Fig. 5.4 shows the GNU blocks designed for data collection.

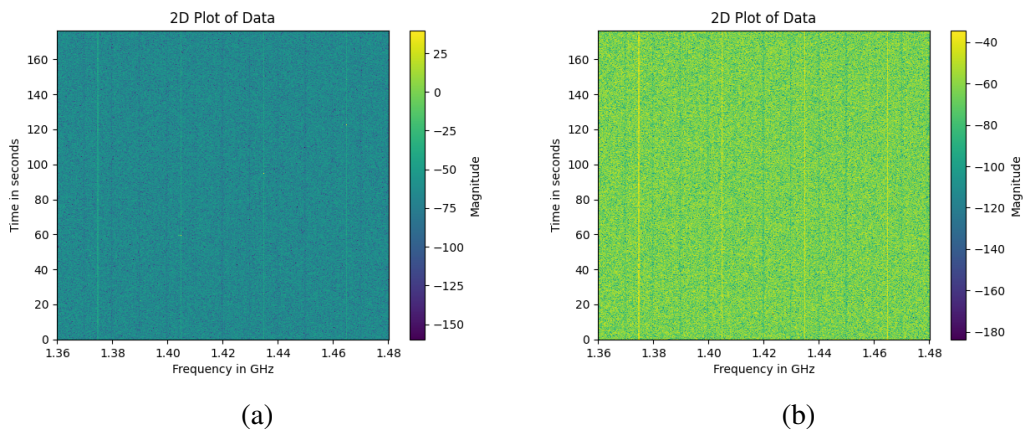


Figure 5.3: (a) Data taken inside Anechoic Chamber (b) Data taken outside Anechoic Chamber

Fig. 5.3 shows the plot of the signal received by the patch antenna in the lab setup. Fig. 5.3a shows the data collected inside an anechoic chamber, that is free of any noise. Fig. 5.3b shows data collected outside the chamber, indicating signal noise from the surrounding environment. The RFIM is set to gather data in Low Earth Orbit (LEO), aiding in the mapping of areas with and without noise. The selection of the RFI investigation frequency is subject to change depending on the requirement of RFI mapping.

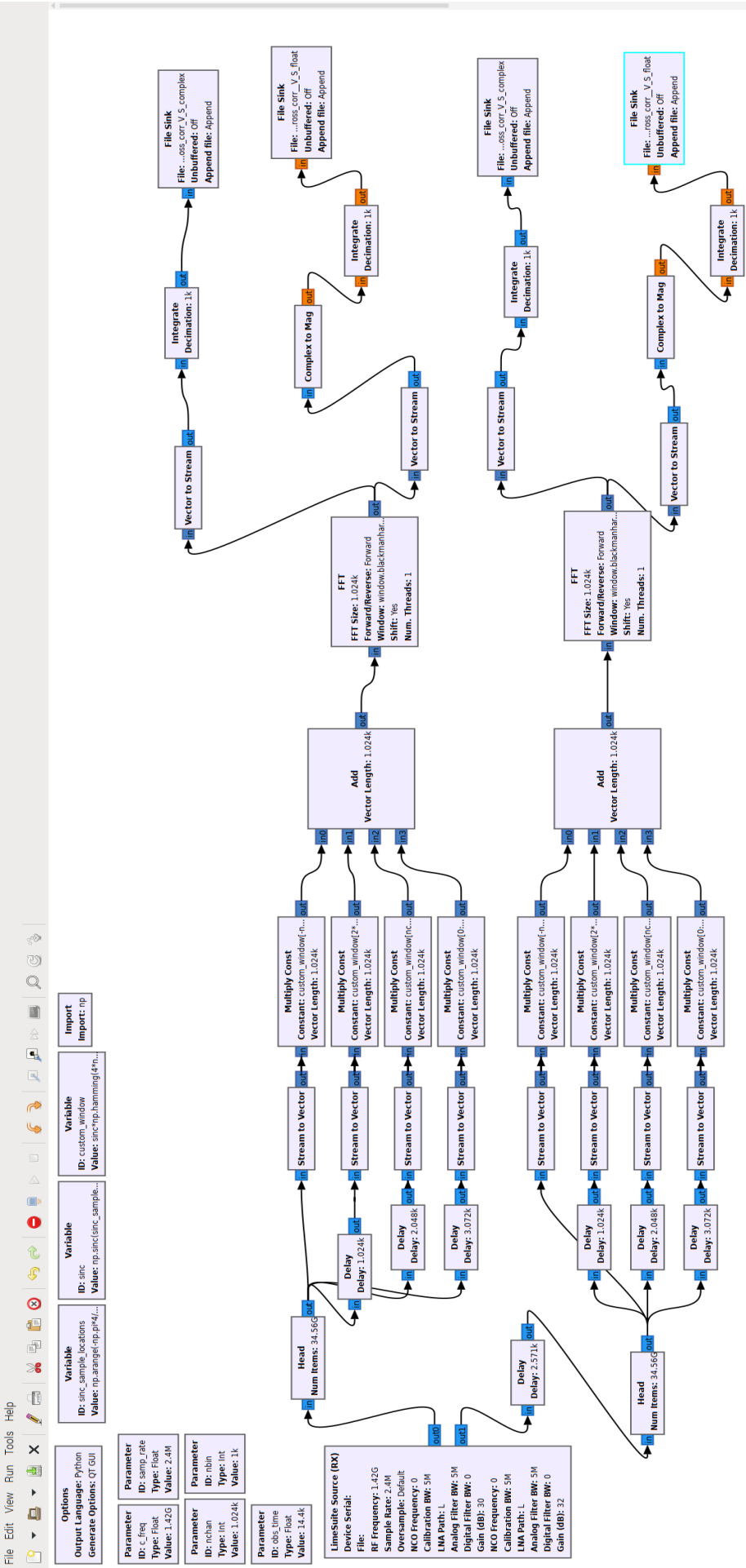


Figure 5.4: GNU blocks for RFIM

## 5.2 Radio Interferometer:

### 5.2.1 Block Diagram:

Fig. 5.5 depicts a basic flow graph of the two-element interferometer. The data acquisition process in a basic two-element interferometer begins with the antennas. Each antenna (antenna 1 and antenna 2) captures the incoming radio waves from the celestial source of interest.

To amplify these weak signals, they are then fed into separate Low-Noise Amplifiers (LNAs) having a gain of 40dB and a noise figure of nearly 1.05 dB. These amplifiers boost the signal strength without introducing significant noise, making it easier to process the data in the following stages.

Following amplification, each signal passes through a dedicated Band-Pass Filter (BPF). These filters act like gates, allowing only radio waves within a specific frequency range to pass through. Here, the filter is however used for blocking DC output from the LNA.

A radio interferometer evaluates the mutual coherence function of the electric field produced by a particular source's brightness distribution in the sky. The interferometer's antennas transform electric fields into voltages. The mutual coherence function is calculated by cross-correlating the voltages from each pair of antennas. Here we have used an FX correlator where the Fourier transform is taken before multiplication. A schematic of an FX correlator is shown in Fig. 5.6.

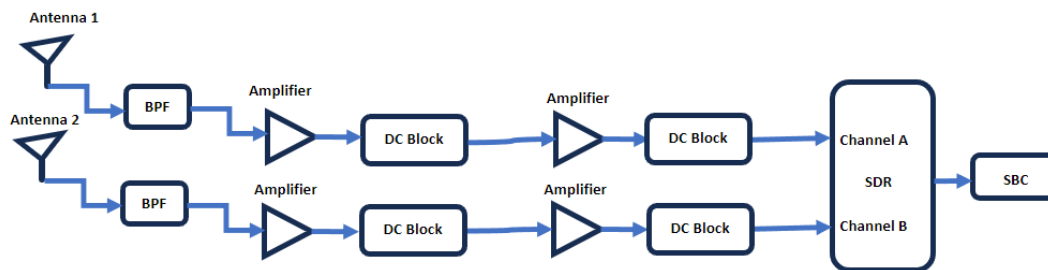


Figure 5.5: Basic Interferometer block diagram

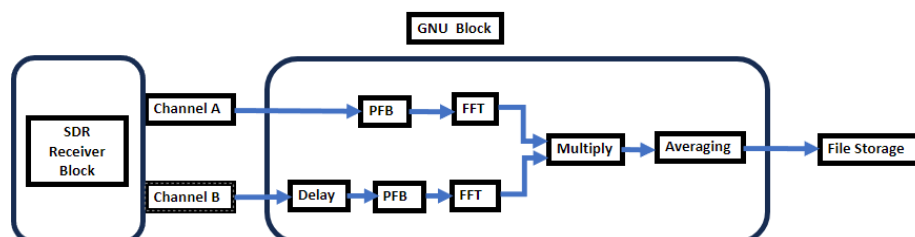


Figure 5.6: GNU flow diagram

A brief of the blocks used is as follows:

- **Delay:** Delay adjustments were implemented to synchronize the signals, compensating for the variation in wire/instrument delay caused by the difference in distance between the two antennas.
- **Polyphase Filter Bank (PFB):** A polyphase filter bank is a signal processing technique used to divide a signal into multiple frequency bands or channels. It achieves this by splitting the input signal into several parallel paths, each associated with a different phase of a filter. As shown in Fig. 5.7, The time series  $x(i)$ , consisting of 1024 samples, are multiplied point by point with a window function  $w(i)$  (a sinc function) of the same length. The resulting product is divided into 4 blocks, each containing 256 samples, and then added together [11].

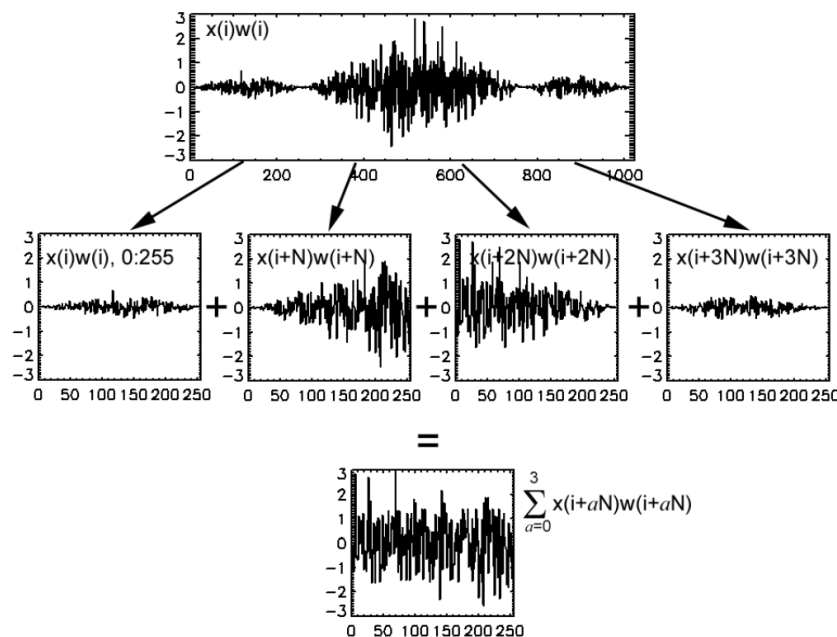


Figure 5.7: Graphical depiction of polyphase filtering [11]

The key advantage of a polyphase filter bank is its efficiency in processing signals with multiple frequency components. By dividing the signal into separate frequency bands, each filter in the bank can focus on processing a narrower portion of the spectrum, reducing computational complexity and improving overall performance.

- **Fast-Fourier Transform (FFT):** The core component of the F-engine is the Fast Fourier Transform (FFT) block, responsible for converting the time-domain data into Fourier coefficients, or spectra. The FFT calculates:

$$X(k) = \sum_{n=0}^{N-1} x(n)e^{-\frac{2\pi jnk}{N}} \quad (5.1)$$

This equation transforms the time-domain signal  $x(n)$  into its corresponding frequency-domain representation  $X(k)$ .

The FFT utilized in this design consists of 1024 points. As the data remains 4-to-1 time-multiplexed after passing through the polyphase FIR filter, it is organized into blocks of length 1024 from the same channel before being inputted into the FFT.

- **Multiply Block:** The signals from the two antennas are multiplied together, which effectively computes the cross-correlation between them.
- **Averaging:** The cross-correlated signals from each frequency bin are integrated over time. Fig. 5.8 shows the GNU block designed for interferometer testing and data collection.

## 5.2.2 Phase Calibration

The process starts by verifying the functionality of the digital backend, the software and processing system that handles the digitized radio signals. Any time delays introduced by the electronics within the instrument are identified and calibrated. These delays can arise from variations in cable lengths, processing times, or other electronic components leading to phase mismatch between the signals. These phase mismatches should be avoided.

The ideal scenario for phase calibration involves a plane wave arriving directly overhead (from the zenith). A plane wave is a theoretical wavefront with a constant phase across its surface. When a plane wave from directly overhead hits the antennas, it arrives "in phase," meaning the peaks and troughs of the wave signal coincide for both antennas. Additionally, if the cables connecting the antennas to the correlator (the point marked "X" as shown in fig.5.9a, where the signals are multiplied) have the same length, the signals from both antennas will reach the correlator at exactly the same time, further contributing to a "maximum response."

To account for potential phase mismatches within the instrument itself (not related to cable lengths), a signal generator is used. The signal from the generator is fed to both LimeSDR-USB boards (presumably the core of the interferometer) through a power splitter, ensuring identical signals reach each channel of the board. Fig. 5.9a depicts the components used to minimize the phase difference between the two identical signals provided by the signal generator. Fig. 5.9b shows the measured phases of the two signals after adjustments, ideally achieving a zero or minimal phase difference.

## 5.2.3 Backend Testing

The initial testing of the instrument's back-end system (Fig.5.10), responsible for processing digital signals, was conducted using a horn antenna as shown in Fig.5.11. This antenna resonates at a frequency of 1.42 GHz and has a beam width of  $\sim 35^\circ$ . Multiple tests and gain adjustments were carried out and data was collected capturing

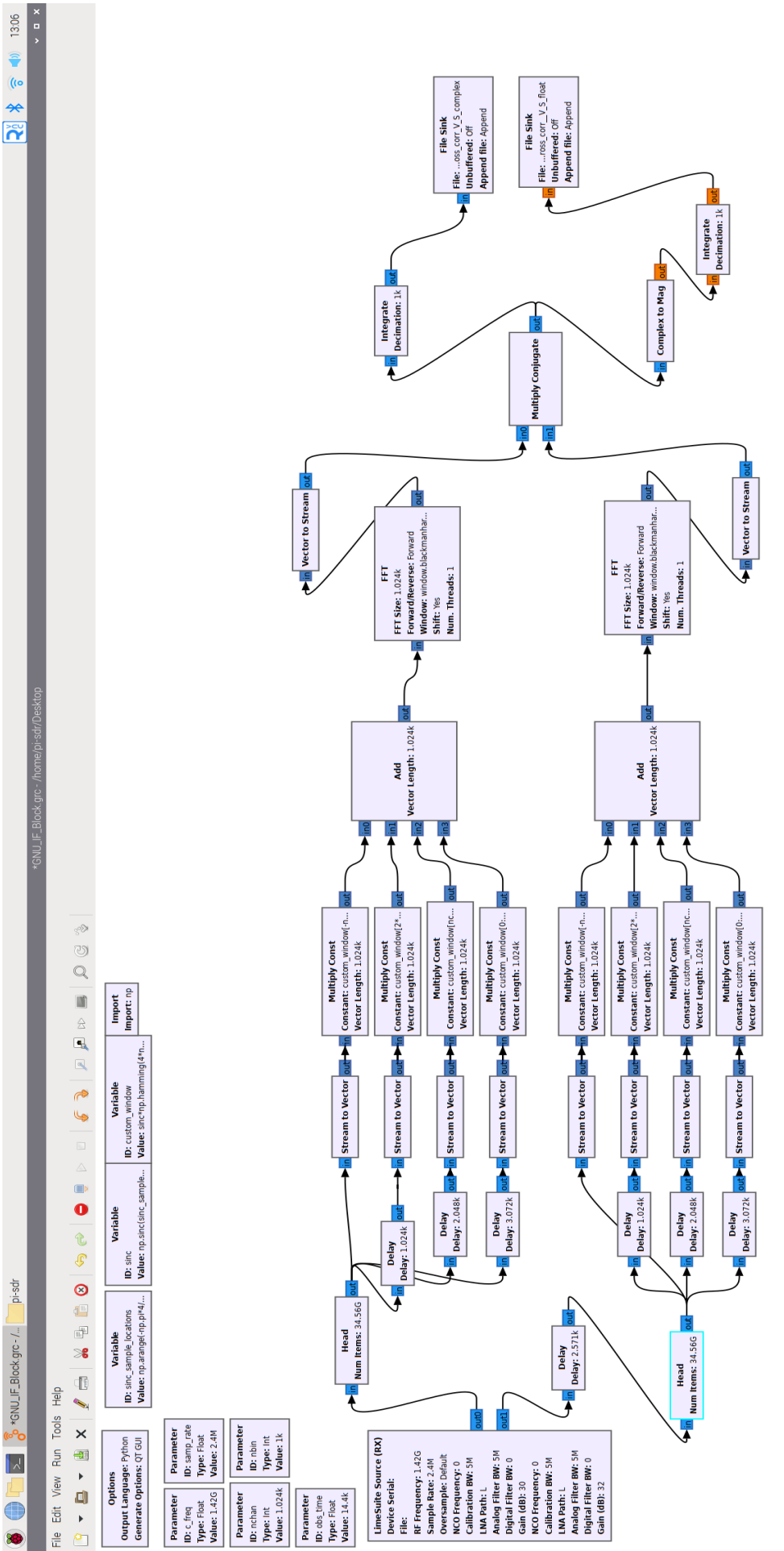


Figure 5.8: GNU blocks for Interferometer

```
<<< Welcome to GNU Radio Companion 3.10.9.0-rc1 >>>
Block paths:
/usr/local/share/gnuradio/gc/blocks
Loading: /home/pi-sdr/Desktop/GNU_IF_Block.grc
>>> Done
```

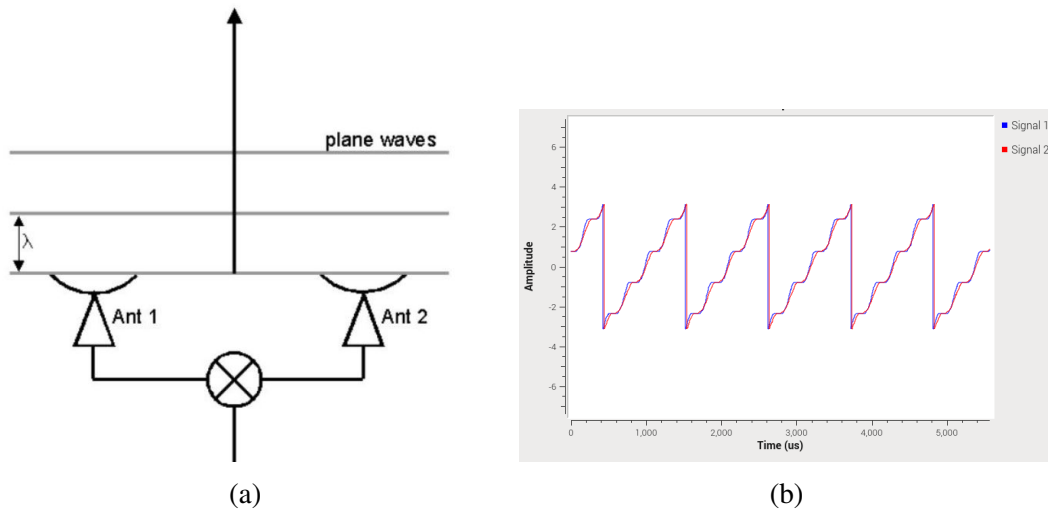


Figure 5.9: (a) Interferometer's baseline geometry, with plane waves arriving vertically (b) Phase vs Amplitude graph

the sun's transit. Both antennas were directed towards the sky, positioned at an azimuth of  $240^\circ$  and an elevation of  $63^\circ$ , having an effective baseline of 4 meters.

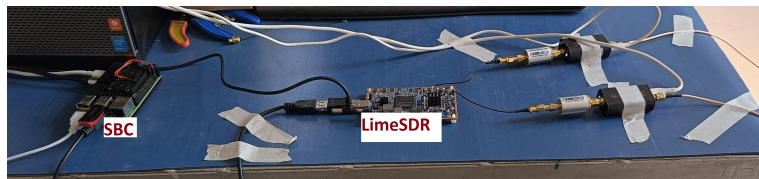


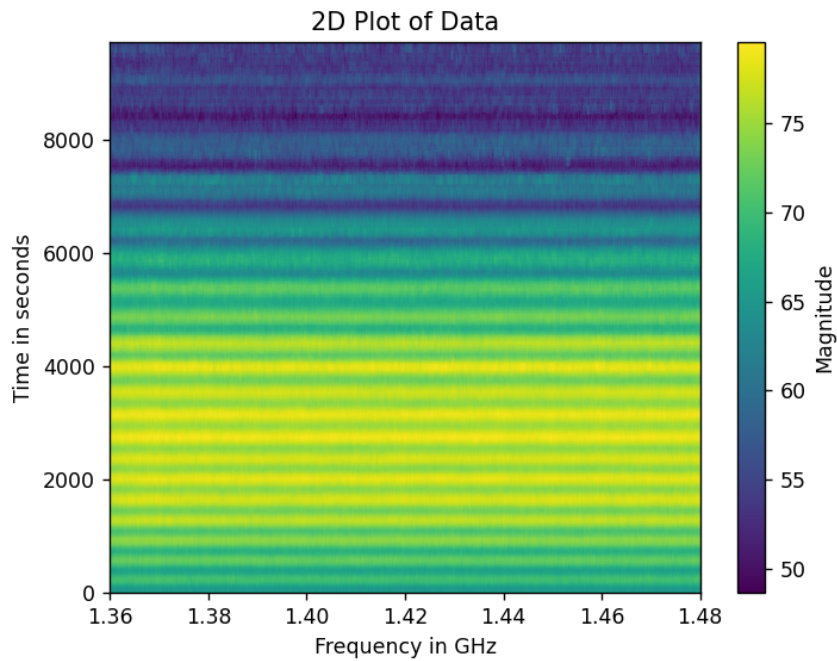
Figure 5.10: Backend Components: SDR and SBC Integration



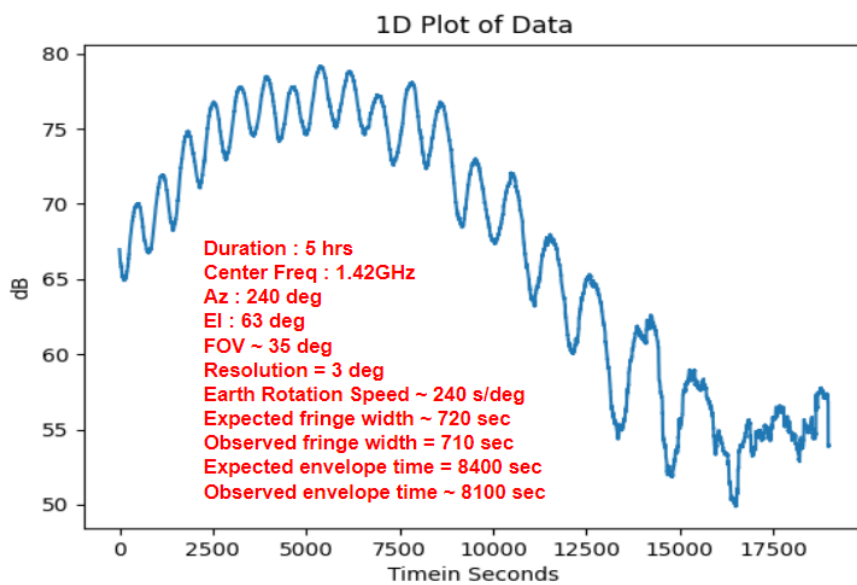
Figure 5.11: Setup of a Two-Element Interferometer with Horn Antennas

## Result

The duration of the recording session was 5 hours, with a center frequency of 1.42GHz. With the effective baseline of 4m, the resolution was 3 degrees (1.13). Given the Earth's rotation speed of approximately 240 seconds per degree, the expected fringe width was calculated to be around 720 seconds.



(a)



(b)

Figure 5.12: (a) 2D plot of data (b) Fringe pattern plot

The analysis of the plots Fig.5.12 confirms the successful design of the interferometer's backend system. The plots likely display a pattern of fringes, which are fluctuations in the signal strength caused by the constructive and destructive interference of radio waves arriving at the antennas with a slight time difference. The presence of fringes indicates that the backend is effectively combining and processing the signals from both antennas.

#### 5.2.4 On field test with patch antenna

After the successful completion of back-end testing, the back-end configuration was retested using the CubeSat setup with a patch antenna, as illustrated in Fig. 5.13.



Figure 5.13: Test setup using patch housed by 3D printed CubeSat structure

In this setup, the 2U structure accommodates one antenna and the back-end system, while the 1U structure accommodates the other antenna along with tether materials.

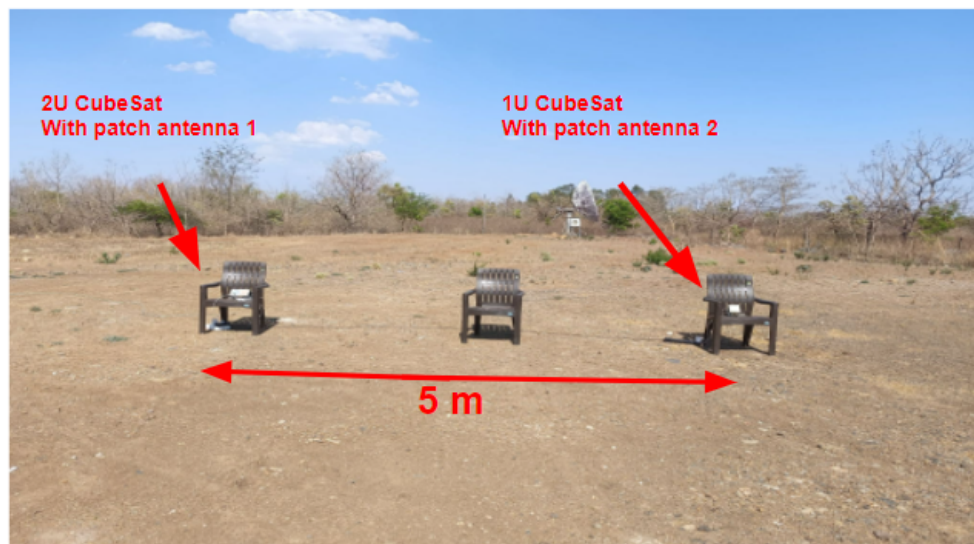


Figure 5.14: Setup of a Two-Element Interferometer with Patch antennas

#### Result

Patch antenna results weren't ideal. Although some fringe-type pattern is being seen in Fig. 5.15, the details are very faint. It's challenging to distinguish these faint

fringes from background noise (RFI) or potentially other fringe patterns. Although the antenna is likely pointed towards the sun, its broader reception area also captures radio frequency interference (RFI) from the surrounding environment. This additional noise masks the subtle fringes caused by the desired radio waves from the sun.

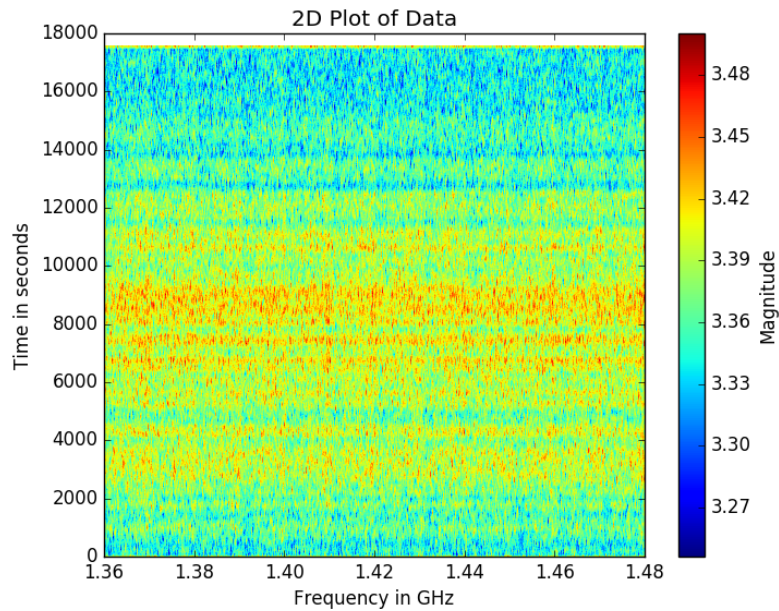


Figure 5.15: 2D plot of patch data

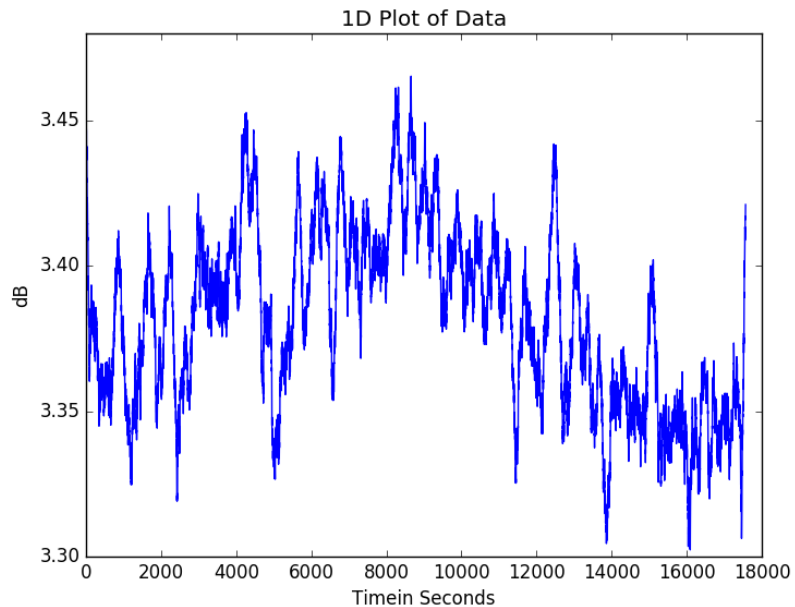


Figure 5.16: 1D plot of patch data

# Chapter 6

## Conclusion and Future Scope

### 6.1 Conclusion

This study proposes a mission utilizing CubeSats, a small and cost-effective spacecraft, inspired by the SEAMS mission. SEAMS aims to survey RFI and test interferometric principles. The proposed mission involves observing RFI scenarios and conducting interferometry using a tethered CubeSat system. This setup comprises a 2U and 1U CubeSat launched as a combined 3U payload into LEO, with the 1U CubeSat deploying autonomously upon reaching orbit. The main goal is to validate the electronic functionality of the tethered system for radio interferometry in astronomical observations. The study includes FEA analysis of the CubeSat structure, configuration of a Two-Element interferometer, and the design of backend processing to observe interferometric fringes. The project made significant progress across multiple fronts. Firstly, Finite Element Analysis (FEA) was utilized to confirm the structural robustness of the CubeSats. Additionally, successfully designed and developed a Radio Frequency Instrument (RFRI) comprising both an RFI meter for quantifying radio interference and a radio interferometer instrument for precise observations. Furthermore, a digital backend system was devised and thoroughly tested to handle signal processing tasks effectively. However, a notable challenge emerged during the testing phase concerning the patch antenna intended for both RFI measurement and interferometry. Initial findings suggested that the antenna's wider beam width might inadvertently capture excessive RFI, potentially masking the desired interferometric fringes.

### 6.2 Future Scope

- A key area of focus is developing a patch antenna with a narrow beam width. This will improve signal reception and reduce unwanted radio frequency interference (RFI), a critical factor for successful interferometry. The design will strictly adhere to the size and weight constraints of the CubeSat form factor.
- Enhancing the capabilities of the tethered CubeSat system for radio interferometry in astronomical observations

- Achieving flight readiness for the tethered CubeSat system.
  - **Telemetry, Tracking, and Command & Control (TTCH):** This subsystem acts as the lifeline between the CubeSat and ground control. It facilitates:
    - \* **Telemetry:** Downlinking data from the CubeSat back to Earth, providing information on its health, performance, and scientific measurements.
    - \* **Tracking:** Monitoring the CubeSat's position and orbit in space.
    - \* **Command & Control:** Sending commands from Earth to control the CubeSat's operations, such as turning on instruments or changing their orientation.
  - **Attitude Determination and Control System (ADCS):** This subsystem plays a critical role in keeping the CubeSat pointed in the right direction.
    - \* **Attitude Determination:** Using sensors (like magnetometers and sun sensors) to determine the CubeSat's current orientation in space.
    - \* **Attitude Control:** Employing actuators (like thrusters or reaction wheels) to maneuver the CubeSat and achieve the desired orientation for its scientific observations or communication with Earth.
  - **Electrical Power System (EPS):** This subsystem is the heart of the CubeSat, responsible for:
    - \* **Power Generation:** Converting solar energy from the sun's rays or other sources (if applicable) into usable electrical power.
    - \* **Power Distribution:** Distributing the generated power to all the CubeSat's subsystems, ensuring they have sufficient energy to function.
    - \* **Power Regulation:** Maintaining a stable and regulated voltage supply for the various electronic components within the CubeSat.

# Bibliography

- [1] California Polytechnic State University, “CalPoly-CDS-Rev.13, CubeSat Design Specification,” California Polytechnic State University, San Luis Obispo, CubeSat Design Specification Rev.13, 2014.
- [2] J. M. Marr, R. L. Snell, and S. E. Kurtz, *Fundamentals of radio astronomy: observational methods*. CRC Press, 2015.
- [3] A. Arbabi and S. Safavi-Naeini, “Maximum gain of a lossy antenna,” *IEEE Transactions on Antennas and Propagation - IEEE TRANS ANTENNAS PROPAGAT*, vol. 60, pp. 2–7, 01 2012.
- [4] M. Mirghani, “Reuse of obsolete dish antenna in radio astronomy,” 01 2017.
- [5] A. Jablonski, G. James, and A. Misra, “Canadian experience in space tethers - an overview,” 09 2011.
- [6] M. Cosmo and E. Lorenzini, “Tethers in space handbook,” 01 1998.
- [7] Lime Microsystems, “LimeSDR-USB hardware description,” [https://wiki.myriadrf.org/LimeSDR-USB\\_hardware\\_description](https://wiki.myriadrf.org/LimeSDR-USB_hardware_description), Date Accessed.
- [8] S. Abdelghafar, A. Darwish, and A. E. Hassanien, “Intelligent health monitoring systems for space missions based on data mining techniques,” *Machine learning and data mining in aerospace technology*, pp. 65–78, 2020.
- [9] A. Yilmaz, “Programming the attitude control of a cubesat for simulation of leo orbit space missions,” B.S. thesis, Universitat Politècnica de Catalunya, 2023.
- [10] A. Lahrichi, “Heat transfer modeling and simulation of masat1,” 05 2017.
- [11] J. L. Losh, “Digital signal processing hardware for a fast fourier transform radio telescope,” Ph.D. dissertation, Massachusetts Institute of Technology, 2012.
- [12] J. D. Monnier, “Stellar interferometry: visible and infrared,” *Reports on Progress in Physics*, vol. 66, no. 5, p. 789, 2003.
- [13] D. F. Buscher, *Principles of long baseline stellar interferometry*. Cambridge University Press, 1999.

- [14] A. Quirrenbach, “The development of astronomical interferometry,” *Experimental Astronomy*, vol. 26, no. 1, pp. 49–63, 08 2009. [Online]. Available: <https://doi.org/10.1007/s10686-009-9166-5>
- [15] M. Colavita, M. Shao, and M. Rayman, “Orbiting stellar interferometer for astrometry and imaging,” *Applied optics*, vol. 32, no. 10, pp. 1789–1797, 1993.
- [16] C. Fridlund, “Darwin-the infrared space interferometry mission,” *ESA bulletin*, vol. 103, no. 3, pp. 20–25, 2000.
- [17] D. A. Quinn and D. C. Folta, “A tethered formation flying concept for the specs mission,” in *Guidance and Control Conference*, no. AAS-00-015, 2000.
- [18] F. D. Lind, P. J. Erickson, M. Hecht, M. Knapp, G. Crew, R. Volz, J. Swoboda, F. Robey, M. Silver, A. J. Fenn *et al.*, “Aero & vista: Demonstrating hf radio interferometry with vector sensors,” 2019.
- [19] J. Burns, G. Hallinan, J. Lux, A. Romero-Wolf, T.-C. Chang, J. Kocz, J. Bowman, R. MacDowall, J. Kasper, R. Bradley *et al.*, “Farside: a low radio frequency interferometric array on the lunar farside,” *arXiv preprint arXiv:1907.05407*, 2019.
- [20] Y. Chen, R. Huang, X. Ren, L. He, and Y. He, “History of the tether concept and tether missions: a review,” *International Scholarly Research Notices*, vol. 2013, 2013.
- [21] R. Hoyt, T. Newton, I. Barnes, J. Shepherd, S. S. Frank, J. Slostad, B. Jaroux, R. Twiggs *et al.*, “Early results of the multi-application survivable tether (mast) space tether experiment,” 2007.
- [22] M. Nohmi, “Development of space tethered autonomous robotic satellite,” in *2007 3rd International Conference on Recent Advances in Space Technologies*. IEEE, 2007, pp. 462–467.
- [23] K. Konstantinidis and R. Förstner, “Cuballute: A cubesat mission to deploy an inflatable hypersonic drag body (ballute) in the martian atmosphere,” 10 2013.
- [24] M. B. Quadrelli and E. C. Lorenzini, “Precision tethered formations for leo and space interferometry applications,” 2001.
- [25] A. Brunello, L. Olivieri, G. Sarego, A. Valmorbida, E. Lungavia, and E. C. Lorenzini, “Space tethers: parameters reconstructions and tests,” in *2021 IEEE 8th International Workshop on Metrology for AeroSpace (MetroAeroSpace)*. IEEE, 2021, pp. 235–240.
- [26] M. B. Quadrelli, F. Y. Hadaegh, M. Shao, and E. C. Lorenzini, “Formations of tethered spacecraft as stable platforms for far ir and sub-mm astronomy,” *New Concepts for Far-Infrared and Submillimeter Space Astronomy*, 2004.

- [27] H. A. Tanti, A. Datta, and S. Ananthkrishnan, "Snapshot averaged matrix pencil method (sam) for direction of arrival estimation," *Experimental Astronomy*, vol. 56, no. 1, pp. 267–292, 2023.
- [28] P. Murugan, "Satellite projects by indian students," *PES*, vol. 1, p. C34, 2016.
- [29] M. L. Cosmo and E. C. Lorenzini, "Tethers in space handbook," Tech. Rep., 1997.
- [30] K. Konstantinidis and R. Förstner, "Cuballute: A cubesat mission to deploy an inflatable hypersonic drag body (ballute) in the martian atmosphere," 10 2013.
- [31] J. Pearson, E. Levin, J. Oldson, and H. Wykes, "Lunar space elevators for cislunar space development," Retrieved from NASA Institute for Advanced Concepts: [http://www.niac.usra.edu/files/studies/final\\_report/1032Pearson.pdf](http://www.niac.usra.edu/files/studies/final_report/1032Pearson.pdf), 2005.
- [32] J. Querol, A. Perez, and A. Camps, "A review of rfi mitigation techniques in microwave radiometry," *Remote Sensing*, vol. 11, no. 24, 2019. [Online]. Available: <https://www.mdpi.com/2072-4292/11/24/3042>
- [33] B. Yu, H. Wen, and D. Jin, "Review of deployment technology for tethered satellite systems," *Acta Mechanica Sinica*, vol. 34, pp. 754–768, 2018.
- [34] A. Raslan, G. Michna, and M. Ciarcià, "Thermal simulation of a cubesat," in *2019 IEEE International Conference on Electro Information Technology (EIT)*. IEEE, 2019, pp. 453–459.
- [35] C. Güvenç, B. Topcu, and C. Tola, "Mechanical design and finite element analysis of a 3 unit cubesat structure," *Machines. Technologies. Materials.*, vol. 12, no. 5, pp. 193–196, 2018.
- [36] J. Herrera Arroyave, J. Ferrer-Pérez, A. Colin, and B. Bermúdez-Reyes, "Cubesat system structural design," 09 2016.
- [37] C. Johnson and P. Wilke, "Protecting satellites from the dynamics of the launch environment," in *AIAA Space 2003 Conference & Exposition*, 2003, p. 6266.
- [38] D. Bhalla and K. Bansal, "Design of a rectangular microstrip patch antenna using inset feed technique," *IOSR Journal of Electronics and Communication Engineering*, vol. 7, no. 4, pp. 08–13, 2013.